Politecnico di Torino

Politecnico di Torino

Master Degree Thesis in Aerospace Engineering

A.a. 2025/2026

Graduation Session December 2025

Characterization of dielectric barrier discharge plasma actuators for drag reduction

Supervisors:

Jacopo Serpieri

Edoardo Fracchia

Candidate:

Alessandro Gallo

Abstract

The environmental impact of the aviation sector has prompted significant research efforts aimed at developing strategies to reduce aircraft aerodynamic drag. In particular, it is estimated that 50% of the overall drag for a medium sized civil aircraft is caused by skin friction drag. In order to reduce it, many active and passive flow control techniques are currently being studied and have been employed in recent years. The primary means to achieve drag reduction is to interact with and disrupt the coherent turbulent structures, thus suppressing the regeneration and self-sustaining mechanisms typical of wall-bounded turbulence. One of these active techniques involves the use of dielectric barrier discharge plasma actuators (DBD-PAs). These devices ionize and accelerate the fluid that surrounds the exposed electrode, generating a controlled wall jet flow. They are particularly versatile due to their simple design, low weight and reduced size, as well as their moderate manufacturing cost. In addition, as an active flow control technique, they offer the ability to adapt to a wide range of operating conditions.
In this thesis project, a non traditional configuration of actuators with sinusoidal shaped electrodes was designed and constructed. The manufacturing process is also innovative, offering higher precision and faster production compared to previously used techniques, and involves the use of a stencil laser-cut into geometries of arbitrary complexity, which is then brushed with conductive paint. The DBDs operate in continuous mode and, thanks to their geometry, create a standing wave configuration capable of producing colliding wall jets between the exposed electrodes. Subsequently, the actuators were characterized with respect to their body force generation and electrical response, as well as power consumption. The experimental measurements were conducted using cross-flow Stereo Particle Image Velocimetry (S-PIV) techniques inside a boundary layer wind tunnel, while the electrical characterization process was mainly carried out with direct voltage and current readings obtained from an oscilloscope.
All activities were conducted at the Laboratory of Aeronautics "M. Panetti" of Politecnico di Torino.

Acknowledgements

Table of Contents

List of Figures

Chapter 1

Introduction

The aerospace sector is undoubtedly one of the main contributors to global pollution due to massive emissions of CO, CO_2, nitrogen oxides, soot, unburnt hydrocarbons, and H_2O [1]. These chemical species are harmful to both humans and the environment, as they include greenhouse gases and substances that deplete the ozone layer[1]. Therefore, it is important to aim to reduce fuel consumption, also to achieve an economic benefit, since fuel is one of the largest contributors to aircraft operating costs.
For a conventional aircraft, the fuel consumption is closely related to the aerodynamic drag of the airplane. In fact, the following formulas apply:

$$\dot{m}_f = TSFC \cdot T \tag{1.1}$$

$$T \approx D \tag{1.2}$$

where $\dot{m}_f$ is the fuel mass flow rate and $TSFC$ is the specific fuel consumption. T is the necessary thrust produced by the engines to counteract D (total drag of the aircraft) and guarantee a leveled flight.
So, it is important to find new ways to reduce the aerodynamic drag. On an aircraft, the total aerodynamic drag is given by the sum of three components:

- Induced drag: it originates from the pressure distribution around the aircraft.
- Skin–friction drag: it is generated by the shear stresses that develop at the wall due to the viscosity and turbulence of the fluid.
- Wave drag: it appears when the aircraft moves near or above the speed of sound. It is caused by the formation of shock waves, which create large pressure differences around the body.

In this research activity, the focus has been placed on reducing skin-friction drag.

1.1 Turbulent flows

In practical applications, the flows of greatest engineering interest are turbulent flows. These can be classified into confined flows, also called wall-bounded flows, which are constrained by solid boundaries, such as boundary layers over a flat plate or an aircraft wing, as well as flow inside pipes, channels, or ducts. Alternatively, there are free shear flows, which are not directly constrained by walls, such as free jets, wakes behind bluff bodies, and mixing layers.

1.1.1 Boundary layer flow over a flat plate

The case considered in this study involves a flow over a flat plate positioned within a wind tunnel.

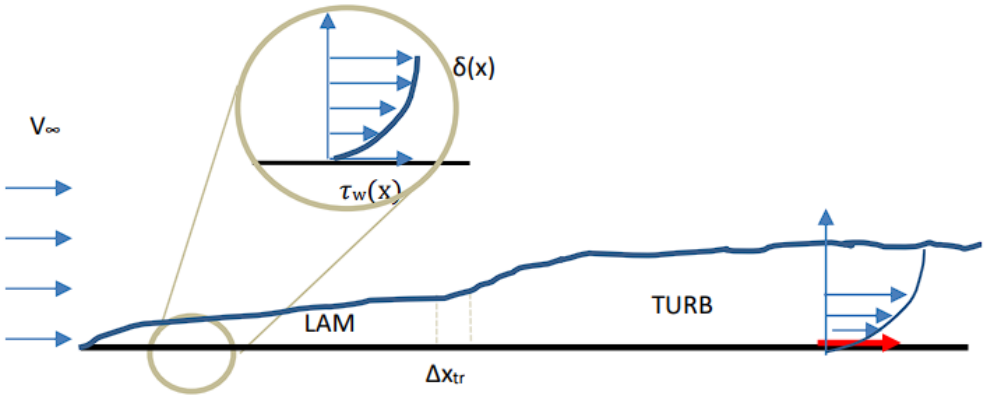

Figure 1.1: Boundary layer over a flat plate.

The flow field is governed by the Reynolds number, and, depending on its local value $Re_x = \frac{U_\infty \cdot x}{\nu}$, where, in this case, x is the streamwise location of the considered point of measure, U_∞ is the free stream velocity and ν is the kinematic viscosity of the fluid. the boundary layer can be either laminar or turbulent. The boundary layer is considered turbulent when the Reynolds number is at least $5 \cdot 10^5$. For a given plate length L and upstream flow velocity U_∞, it is possible to define the global Reynolds number of the plate:

$$Re_L = \frac{U_\infty \cdot L}{\nu} \tag{1.3}$$

The ratio between the local and global Reynolds numbers allows for estimating the transition location along the flat plate:

$$\frac{x_{tr}}{L} = \frac{5 \cdot 10^5}{Re_L} \tag{1.4}$$

In the case of a laminar boundary layer, the solution of the governing equations leads to the Blasius solution, which defines the following dimensionless velocity profile:

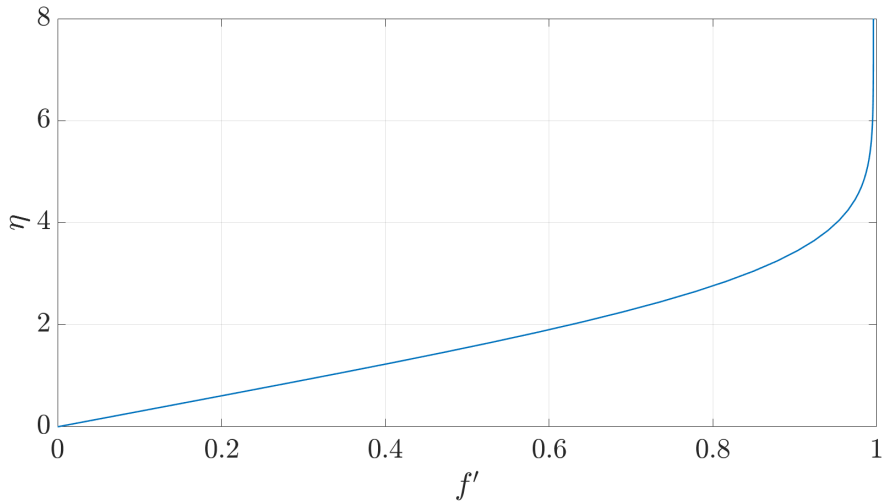

Figure 1.2: Typical solution for a blasius boundary layer over a flat plate, $U_\infty = 15$ m/s.

$$f'''(\eta) + \frac{1}{2} f(\eta) f''(\eta) = 0, \quad u = U_\infty f'(\eta), \quad \eta = y\sqrt{\frac{U_\infty}{\nu x}} \tag{1.5}$$

Here, f is the Blasius function, and

$$\frac{u}{U_\infty} = f'(\eta)$$

represents the dimensionless velocity, while η is the similarity coordinate.

On the other hand, if the boundary layer is turbulent, it exhibits a multi-layered structure, mainly consisting of two regions: the inner layer and the outer layer. The

inner layer, which spans approximately (10-20) % of the boundary layer thickness δ, is itself composed of three sublayers: the viscous sublayer, the buffer layer, and the logarithmic layer. The main quantities used to characterize this type of boundary layer are:

$$u_\tau = \sqrt{\frac{\tau_w}{\rho}}, \quad l_\tau = \frac{\nu}{u_\tau}, \quad y^+ = \frac{y}{l_\tau}, \quad U^+ = \frac{U}{u_\tau} \tag{1.6}$$

where y^+ is the dimensionless wall-normal coordinate, u^+ is the dimensionless velocity, l_τ is the viscous length scale, and u_τ is the friction velocity defined from the wall shear stress τ_w and the fluid density ρ.

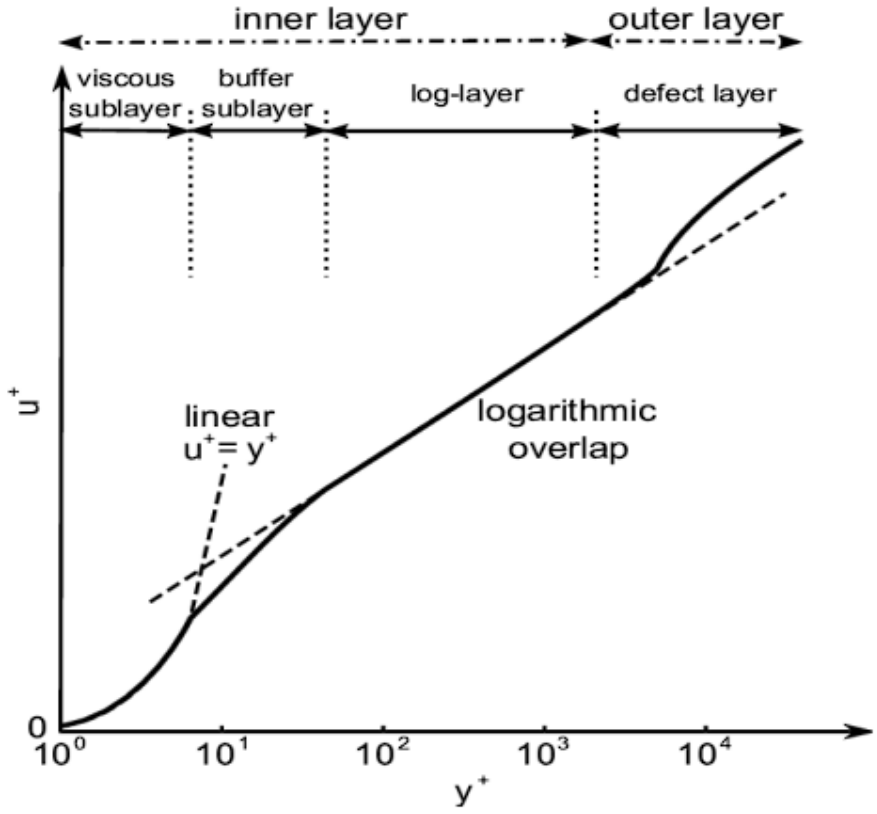

Figure 1.3: Law of the wall for a turbulent boundary layer. Reproduced from [2].

In the viscous sublayer ($y^+ < 5$), viscous forces dominate over inertial forces, and the velocity profile is given by

$$U^+ = y^+ \tag{1.7}$$

which is, a linear trend of the dimensionless velocity with respect to the dimensionless wall-normal coordinate.
In the logarithmic layer ($y^+ > 30$), inertial forces dominate over viscous forces. Here, the velocity profile follows the so-called logarithmic-law:

$$U^+ = \frac{1}{\kappa} \ln(y^+) + C, \tag{1.8}$$

where $\kappa = 0.41$ is the von Kármán constant and C is an empirical constant with tipical value of $C \approx 5.2$ [2].

Between the two regions lies an intermediate transition layer, the *buffer layer* (typically $5 < y^+ < 30$), where viscous and inertial forces are of the same order of magnitude. This region is of particular interest since it is precisely here that the maximum production of turbulent kinetic energy occurs [2].

Outside the inner layer lies the outer layer. It is not possible to formulate a universal law for the velocity distribution in this region, as it strongly depends on the external flow conditions.

1.1.2 Turbulence

Turbulence is a state of fluid motion characterized by random velocity fluctuations that span a wide range of spatial and temporal scales. It is intrinsically a three-dimensional and rotational phenomenon. Moreover, it is a purely dissipative phenomenon, since turbulence, due to the inertial cascade, transfers energy from larger scales to smaller ones, eventually reaching the Kolmogorov scale ($Re \approx 1$), where the kinetic energy is dissipated by viscosity. However, despite the unpredictable and random nature of turbulence, it is possible to identify some coherent structures within it.

1.1.3 Turbulent structures

Turbulent structures or quasi-coherent structures are regions of space and time (significantly larger than the smallest flow or turbulence scales) within which the flow field has a characteristic coherent pattern [2].These structures can be classified as follows:

- **Quasi-streamwise vortices**: They are pairs of elongated, tube-shaped counter-rotating structures that run roughly in the streamwise direction and can be found in the near-wall region ($y^+ < 100$). They are closely associated with streaks and ejection events.

- **Horseshoe vortices**: They consist of a head located in the outer regions of the boundary layer and two legs with oppositely directed vorticity in the viscous sublayer. These vortices can reach very large dimensions, with a total length comparable to the boundary layer thickness δ.

These structures produce the following effects in the fluid:

- **Streaks**: These are elongated flow regions in the streamwise direction. High-speed streaks alternate with low-speed streaks and are found in the viscous sublayer. Streaks exhibit a characteristic behavior known as bursting, which produces the ejections.

- **Ejections**: As the streak moves downstream, it slowly lifts away from the wall until it rapidly detaches, causing the ejection of low-speed fluid from the wall toward the outer layers of the boundary layer.

- **Sweeps**: The opposite phenomenon of ejections, characterized by fluid moving from the outer layers of the boundary layer toward the wall.

1.1.4 Drag reduction methods in turbulent flows

Although the mechanisms of turbulence generation are not yet fully understood, it is now evident that in order to reduce wall friction caused by turbulence, it is necessary to interact in some way with the coherent structures within the boundary layer. The goal is to modify the flow so as to reduce the velocity gradient $\frac{\partial u}{\partial y}$ at the wall, which is directly proportional to the wall shear stress: $\tau_w = \mu \left.\frac{\partial u}{\partial y}\right|_{wall}$.

There are two fundamental approaches to flow control techniques: the passive approach and the active approach.

- Passive techniques: they consist in modifications to the surface geometry directly in contact with the flow, and do not require additional energy for flow control. They are simple to implement, but, due to their inherent nature, they cannot adapt to varying flow conditions. Being optimized for a specific situation, they often become detrimental to performance if operating away from the design point. An example of a passive technique is the use of riblets, i.e., surface roughness elements with dimensions comparable to the viscous sublayer thickness, appropriately shaped and aligned with the flow. Significant results in terms of drag reduction have been achieved using riblets, but they are rather delicate, as contamination by dust or other pollutants can alter their geometry and reduce their effectiveness [3].

- Active techniques: on the other hand, active techniques require an energy input for their operation, but they are generally more effective and can adapt to varying flow conditions as the characteristic parameters change.

  One technique that has achieved considerable success in recent years involves recreating a Stokes layer, i.e., a periodic velocity field transverse to the flow, as illustrated in Figure 1.4.

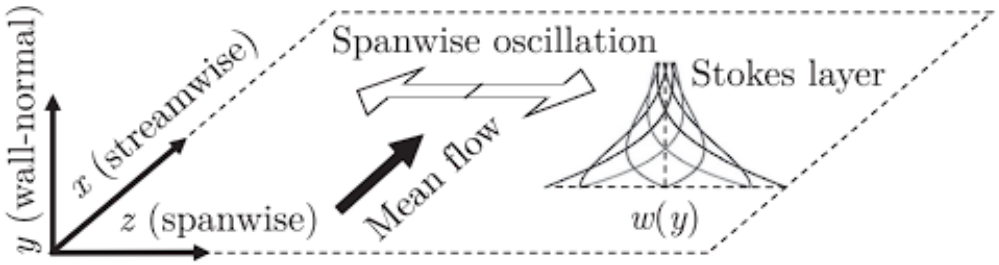

Figure 1.4: Stokes layer generated by spanwise oscillation of the wall; reproduced from [4].

In the simplest actuated configuration, the entire wall oscillates purely in time in the spanwise direction according to equation 1.9:

$$W_w(t) = W_m cos\left(\frac{2\pi t}{T}\right) \tag{1.9}$$

where W_m is the amplitude of the wall velocity, T is the oscillation period and t is the time. The fluid, periodically moving with spanwise velocity, leads to a spanwise shear layer that favorably interacts with near-wall turbulence up to the buffer layer and yields drag reduction [4]. Historically, attempts to recreate the Stokes layer involved physically moving the wall. However, this approach is extremely complex and limited by mechanical inertia and resonant effects and several studies have revealed that in turbulent flows, with the exception of low values of W_m, the actuation power required to oscillate the wall according to equation 1.9, exceeds the power saved by the drag-reduction margin, leading to a negative net energy balance [5].

For these reasons, alternative methods to wall motion have been sought after, ultimately leading to the employment of dielectric barrier discharge (DBD) plasma actuators (PAs). Plasma actuators are active flow-control devices that generate a discharge-based body force in the vicinity of the wall, allowing the

recreation of Stokes layer conditions. Further details regarding their operation will be provided in section 1.2.

1.2 Dielectric barrier discharge plasma actuators

DBD plasma actuators present numerous advantages, such as their robustness (they have no moving or fragile parts) and low cost (the materials are inexpensive and the power consumption is limited). Their main goal, when using these devices for flow control, is to generate laminar wall jets capable of interacting with the boundary layer flow, and, in turbulent flows, modifying the turbulent structures that arise within it. The expected outcomes are several, including the delay of flow separation and turbulent transition or the achievement of a significant reduction in wall shear stresses.

1.2.1 Working principles and configurations

Plasma actuators consist of two adjacent conductive electrodes separated by a dielectric layer. One electrode is exposed to the external flow, while the other is usually encapsulated in insulating material to strengthen the production of the electric field and prevent electrical arcs or plasma formation in regions where they could damage the actuator itself. The electrode width is on the order of millimeters and the total thickness is even smaller.

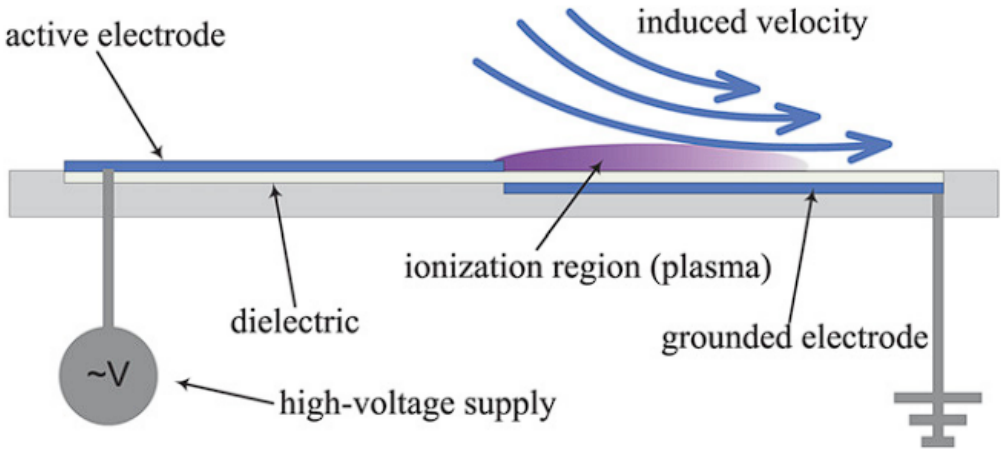

Figure 1.5: Typical geometrical configuration and operation of the plasma actuator; reproduced from [6].

When a sufficient voltage difference is applied to the electrodes, an accumulation

of electric charges and ionized gas occurs near the edge of the exposed electrode, above the encapsulated one. The gas (in plasma form) is subsequently accelerated by the electric field itself, forming a laminar wall jet that is able to entrain the surrounding air through collision mechanisms and momentum exchange between the charged particles and the external flow [7]. This jet, if adequately operated, can induce control motions on the fluid. It should be noted that the device generates a body force that displaces the fluid within its region of influence without introducing any additional mass into the flow. As a consequence, compensating fluid motions towards the wall (recirculation towards the exposed electrode) and toward the outer layers of the boundary layer must occur in order to satisfy mass conservation [6].

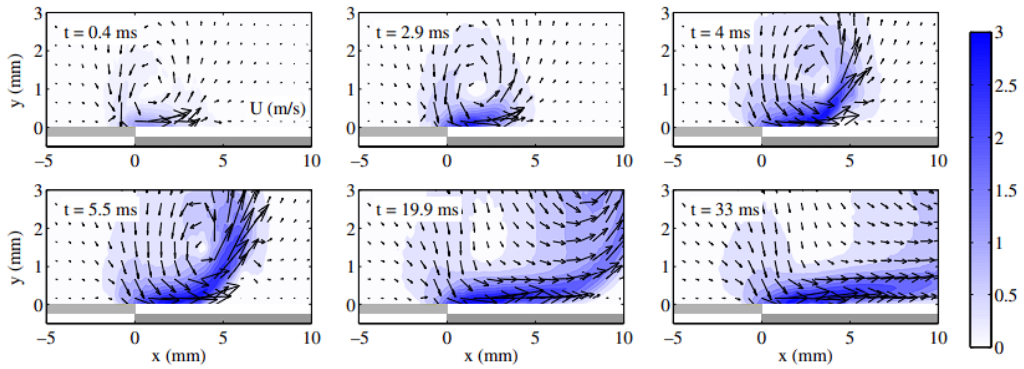

Figure 1.6: Temporal evolution of the total velocity field (U) for the actuation. Fluid movements in the wall normal direction are clearly visible; reproduced from [6].

The operating conditions of a DBD plasma actuator typically lie within a voltage range of 1 kV to 50 kV, while the excitation frequencies vary between 0.5 kHz and 25 kHz. Since the dielectric barrier cannot be crossed by a DC current, an AC signal is required, most commonly in the form of a sinusoidal or square waveform. The main design and operating parameters are the actuator dimensions (length and width of the electrodes), the applied voltage, and the actuation frequency. When creating an array of actuators, the spacing between them also becomes crucial. Finally, when designing an array capable of generating not only unidirectional flows but also oscillating flows (oscillating-wall-like), additional parameters include the modulation period and the duty cycle (DC). In oscillating wall mode, not all electrodes produce plasma simultaneously. Instead, they receive a time-modulated signal such that they generate wall jets that drive the surrounding fluid in both directions alternately (Figure:1.7). This motion is precisely what allows the recreation of the Stokes layer described in Section 1.1.4.

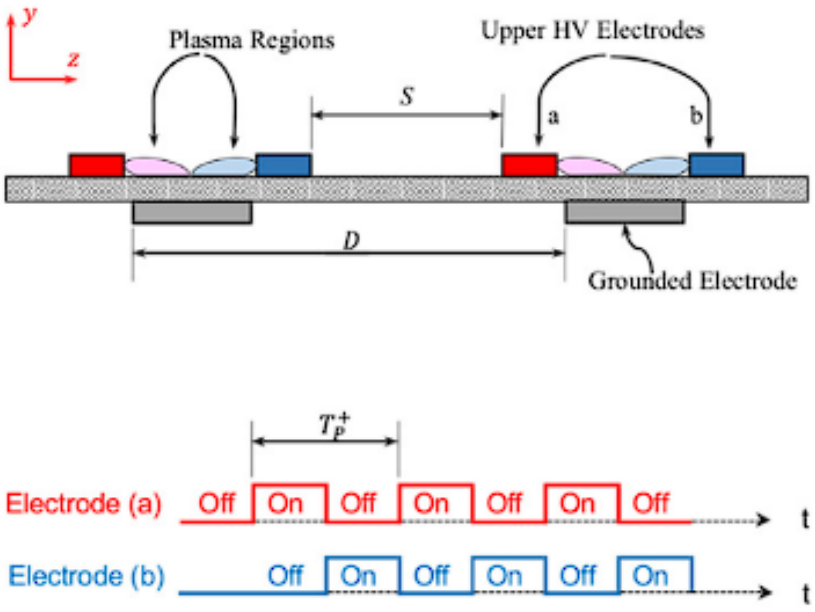

Figure 1.7: cross section of the plasma actuators arrangement for bidirectional wall jets (top) and shape of the applied power signal to operate in oscillating wall mode (bottom); reproduced from [8]

1.3 PAs mechanical characterization

It is crucial to characterize a plasma actuator in terms of the body force it generates, the velocity induced in the flow, and the power consumed. The body force determines the actuator's ability to influence the boundary layer and modify turbulent structures. The induced velocity quantifies the direct effect on the near-wall flow, which is essential for evaluating flow control effectiveness. Finally, the power consumption provides insight into the actuator's efficiency for practical applications, as energy input should be minimized relative to the benefits in drag reduction.

1.3.1 Induced velocity

Measurements for the characterization of the actuators are usually performed in quiescent air. The velocity downstream of a plasma actuator can be measured using an appropriately sized Pitot tube (inner diameter $< 1\,\mathrm{mm}$) with a static pressure port, applying Bernoulli's principle. For quiescent flows, typical velocities of up to $10\,\mathrm{m/s}$ can be reached a few millimeters from the wall, extending

streamwise over a few centimeters. High spatial accuracy is required, and the Pitot tube must be made of non-conductive material to avoid interference with the plasma.

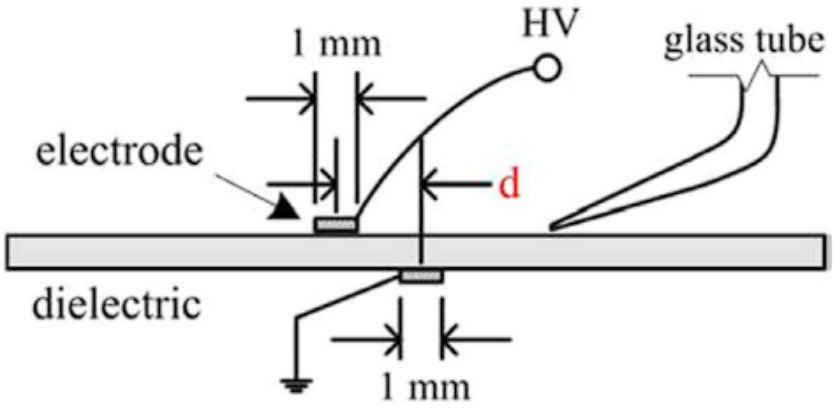

Figure 1.8: Pitot tube measurement setup used by Dong et al; reproduced from [9]

Other methods for the characterization of plasma actuators include the following. Hot-wire anemometry is rarely used due to the risk of electrical arcing between the electrode and the hot wire; in addition, the electromagnetic signal can affect the probe data, also because the flow is slightly heated by the plasma. Laser Doppler Velocimetry (LDV) offers excellent spatial and temporal resolution, with interrogation areas on the order of millimeters. However, this technique suffers from the same problem of measurements performed with a Pitot tube and only provides pointwise measurements. Particle Image Velocimetry (PIV) is the most powerful and suitable method for detailed investigations. However, careful selection of seeding particles is required: they must be appropriate for the flow, but also resistant to dissociation in the plasma and not prone to electrical charging. More details regarding PIV measurements will be provided in Section 2.3. Finally, Schlieren imaging relies on detecting density gradients in the flow, but it only allows visualization of large-scale vortical structures.

1.3.2 Body force

In order to obtain the spatial distribution of the body force generated by a plasma actuator, a time-resolved velocity field is needed. The most widely used approach relies on Particle Image Velocimetry (PIV) measurements. The starting point is given by the incompressible two–dimensional Navier–Stokes equations:

$$\frac{\partial \mathbf{U}}{\partial t} + \mathbf{U} \cdot \nabla \mathbf{U} - \nu \nabla^2 \mathbf{U} = -\nabla p + \frac{\mathbf{F}}{\rho} \tag{1.10}$$

where $\mathbf{U} = (u, v)$ is the velocity vector and $\mathbf{F} = (f_x, f_y)$ is the body force vector generated by the plasma actuator.

Kotsonis et al.[6] proposes two main approaches to estimate the body force generated by plasma actuators:

- **Reduced method**: this approach applies the Navier–Stokes equations (1.10) only during the first instants after the actuator is switched on. In this stage, the flow is expected to accelerate only in the region where the body force is exerted, while the rest of the field remains relatively quiescent. Assuming initial conditions of zero velocity, all the terms relative to the convective, viscous, and pressure gradient can be neglected. The equation therefore reduces to:

  $$\frac{\partial \mathbf{U}}{\partial t} = \frac{\mathbf{F}}{\rho} \tag{1.11}$$

  From this simplified formulation, the body force field can be directly estimated from the temporal rate of change in velocity.

- **Gradient method**: when the full Navier–Stokes equations are considered, it is necessary to compute all terms explicitly. Two simplifying assumptions are required to close the problem: (1) the body force remains quasi-steady over a large number of charge and discharge cycles, and (2) the pressure gradient prior to the actuation is zero. The governing equation (1.10) can now be differentiated in time:

  $$\frac{\partial^2 U}{\partial t^2} + \frac{\partial (U \cdot \nabla U)}{\partial t} - \nu \frac{\partial (\nabla^2 U)}{\partial t} = -\frac{\partial (\nabla p)}{\partial t}\,. \tag{1.12}$$

  It is worth noting that the body force term has disappeared, since in the steady state its time derivative was assumed to be zero. By integrating in time, an expression for the pressure gradient is obtained, which is then substituted into the original Navier–Stokes equation (1.10) to finally determine the body force term $\mathbf{F}$.

  $$\frac{\mathbf{F}}{\rho} = \frac{d\mathbf{U}}{dt} + \mathbf{U} \cdot \nabla \mathbf{U} - \nu \nabla^2 \mathbf{U} - \int_0^t \left(\frac{d\mathbf{U}}{dt} + \mathbf{U} \cdot \nabla \mathbf{U} - \nu \nabla^2 \mathbf{U} \right) dt \tag{1.13}$$

1.3.3 Thrust

Kotsonis et al.[6] also provide this method for calculating the thrust exerted by the actuators on the fluid. Once again, a velocity field in the vicinity of the electrodes, obtained from PIV analysis, is required.
A control volume, where the momentum flux is calculated at the boundaries of the domain and equilibrium with the internal forces is assumed, is defined as shown in Figure 1.9.

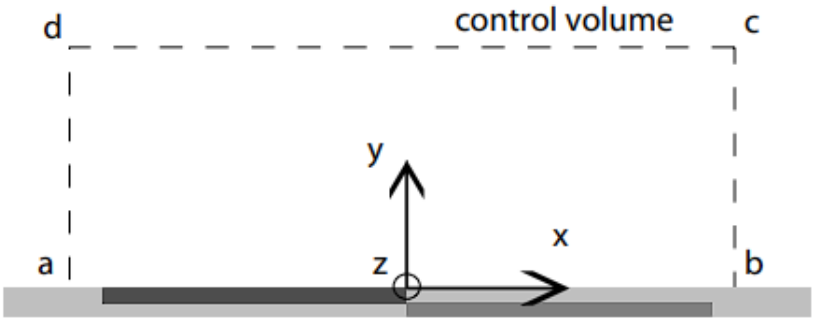

Figure 1.9: The control volume for the momentum balance equations. Reproduced from [6]

Applying the momentum balance equation on the control volume, taking into account the no-slip condition at the wall (no flux across the wall), gives (1.14)

$$\mathbf{T} = \rho \oint_{abcd} (\mathbf{U} \cdot \mathbf{n}) \mathbf{U} d\mathbf{S} + \oint_{abcd} p \, d\mathbf{S} \tag{1.14}$$

where $\mathbf{T}$ is the integrated force exerted on the fluid per unit of depth extension. By decomposing $\mathbf{T}$ into its components along the x and y directions, we have:

$$T_x = \rho \int_{da} u_x^2 \, dy + \rho \int_{cd} u_x u_y \, dx - \rho \int_{bc} u_x^2 \, dy + \int_{da} p \, dy - \int_{bc} p \, dy \tag{1.15}$$

$$T_y = \rho \int_{da} u_x u_y \, dy + \rho \int_{cd} u_y^2 \, dx - \rho \int_{bc} u_x u_y \, dy + \int_{cd} p \, dx - \int_{ba} p \, dx \tag{1.16}$$

As an additional assumption, if the control volume boundaries are sufficiently far from the bulk of the plasma body force, the pressure can be considered uniform and equal along these surfaces. Thus, we obtain (1.17) and (1.18)

$$T_x = \rho \int_{da} u_x^2 \, dy + \rho \int_{cd} u_x u_y \, dx - \rho \int_{bc} u_x^2 \, dy \tag{1.17}$$

$$T_y = \rho \int_{da} u_x u_y \, dy + \rho \int_{cd} u_y^2 \, dx - \rho \int_{bc} u_x u_y \, dy \tag{1.18}$$

Finally, it should be noted that the contribution of the thrust in the x direction includes both the thrust generated by the actuators and that due to wall shear stresses, such that $T_x = T_x^p + T_x^s$. On the other hand, $T_y^s = 0$, so only the effect of the actuator is considered.

from an experimental point of view, the simplest method to estimate the thrust is to connect the actuator to a load cell to measure the force exerted by the induced flow on the actuator. Indeed, according to Newton's third law, the force exerted by the actuator on the flow is equal and opposite to the force exerted by the flow on the actuator. However, the wall jet generated by the electronic device produces wall shear stresses that are also included in the measurement, making it less precise and reliable. Moreover, the results are integrated over the entire actuator surface, providing no spatial information.
Despite these limitations, this technique remains commonly used, at least to assess the order of magnitude of the force exerted.

1.4 Particle image velocimetry

As mentioned in sections 1.3.2 and 1.3.3, in order to compute the body force or the thrust generated by the actuators, it is necessary to measure the velocity field. One of the most powerful and widely used measurement techniques is Particle Image Velocimetry (PIV), which enables the instantaneous acquisition of an entire velocity field. Among the main advantages of this technique, there are its high spatial resolution and its non-intrusive nature. The main components required to perform this type of measurement are:

- **Tracer particles**: they must be suspended in the fluid and have a size small enough to be transported by the flow without altering it. Moreover, their concentration must be sufficiently high and homogeneous to ensure accurate measurements.

- **Laser**: a high–power monochromatic light sheet shaped with a set of lenses. It illuminates a portion of the flow that contains the tracer particles. It is preferable to have the thinnest possible laser sheet in order to obtain meaningful results from the analysis.

- **Camera(s)**: one or more cameras acquire images of the particles illuminated by the laser. The number of pixels $N \times M$ of the recorded images is directly

related to the spatial resolution of the resulting velocity fields. Furthermore, to avoid errors, reflections and additional light pollution must be minimized.

1.4.1 PIV classification

PIV techniques can be classified based on the number of velocity components acquired and the measurement volume considered:

- **Planar PIV 2D2C**: A single camera is sufficient to capture moving particles on a plane. The measured velocity components are two, corresponding to the directions lying within the laser sheet.
- **Stereoscopic PIV 2D3C (sPIV)**: It is possible to measure all three velocity components on a laser-illuminated plane, including the component perpendicular to the plane. At least two cameras are required.
- **Tomographic PIV 3D3C (tPIV)**: Measurements are performed over an entire volume of illuminated particles. All three velocity components can be measured, but this technique is highly complex and typically requires at least three cameras.

PIV can be further distinguished into **time-resolved** and **non-time-resolved**. Time-resolved PIV does not require cameras capable of capturing a large number of frames per second, and, although it does not allow the measurement of the fastest structures typical of turbulent flows (especially at high Reynolds numbers), it provides excellent spatial resolution.

Time-resolved PIV, on the other hand, enables image acquisition at very high frequencies (on the order of tens of kHz), offering excellent temporal resolution. However, more expensive cameras and lasers are required, capable of operating at very high frequencies.

1.4.2 Tracer particles

As discussed earlier in Chapter 2.3, tracer particles are a fundamental component of PIV measurements, since it is the particles themselves, rather than the fluid, which in the case of air is transparent, that scatter the light of the laser. It is therefore essential that they move coherently with the flow and do not alter or disturb it.

The motion of tracer particles is governed by the Basset equation, which in its simplified form can be written as:

$$\left(\frac{\pi D_p^3}{6}\,\rho_p\right)\frac{d\mathbf{u}_p}{dt} = 3\pi\mu_f D_p\left(\mathbf{u}-\mathbf{u}_p\right), \tag{1.19}$$

where D_p, ρ_p, and $\mathbf{u}_p$ represent the diameter, density, and velocity of a particle respectively, while μ_f and $\mathbf{u}$ are the dynamic viscosity and velocity of the fluid.

In order for the particle to float within the fluid, its density must be very close to that of the surrounding medium; otherwise, it would not faithfully follow the flow trajectory ($\rho_f \approx \rho_p$).

Moreover, the particle diameter also plays a crucial role: if it is too small, the light scattered by the particle will be weak and the resulting images will be noisy; conversely, if it is too large, the particle's inertia will prevent it from accurately following the flow motion.

It is therefore possible to introduce a dimensionless parameter, known as the Stokes number (St), which accounts for these considerations. It is defined as:

$$St = \frac{t_p}{t_0}, \tag{1.20}$$

where t_0 represents a characteristic time scale of the flow, while t_p, referred to as the relaxation time, describes the time required for a particle to reach velocity equilibrium with the fluid. The relaxation time is expressed as:

$$t_p = \frac{D_p^2 \, \rho_p}{\mu_f}. \tag{1.21}$$

A particle is suitable for the experiment if the following condition is met:

$$St << 1 \tag{1.22}$$

1.4.3 Data analysis and post processing

In PIV measurements in air, the laser pulses are always synchronized with the cameras, so that images are captured only when the scene is illuminated. Once acquired, the images are divided into small interrogation windows, and, for every window, the objective is to determine the corresponding velocity vector. To achieve this, it is essential that the seeding — that is, the tracer particles — is present in a sufficient number, ideally at least ten particles per interrogation area, in order to obtain a statistically meaningful average of the fluid motion within that region.

Each interrogation window is then compared to the same in the subsequent frame through the cross-correlation function:

$$R_{j,j+1}(r_1, r_2) = \sum_{h=1}^{\Delta h} \sum_{k=1}^{\Delta k} f_j(h,k) \, f_{j+1}(h + r_1, k + r_2) \tag{1.23}$$

where f_j and f_{j+1} are the intensity distributions of the two consecutive images, and (r_1, r_2) denotes the displacement associated with the peak of the correlation

map. Thanks to this correlation function, it is possible to identify the most probable displacement vector $\Delta\mathbf{S}$ within each interrogation window. Knowing the time delay Δt between two consecutive snapshots, the velocity vectors throughout the entire flow field can finally be obtained with:

$$\mathbf{V} = \frac{\Delta\mathbf{S}}{\Delta t} \tag{1.24}$$

1.5 PAs Electrical characterization

1.5.1 Power consumption

It is crucial to determine the actual power consumption of plasma actuators in order to assess whether the energy savings due to drag reduction exceed the energy required to achieve it. There are fundamentally two ways to evaluate the consumed power, as suggested by Kotsonis et al. [10]:

- **Direct evaluation of instantaneous quantities**
  The instantaneous values of voltage $V(t)$ and current $I(t)$ are measured, so that the instantaneous consumed power $P(t)$ is obtained by multiplying them, according to the following relation (1.25):

  $$P(t) = V(t) \cdot I(t) \tag{1.25}$$

  The average power consumption in time can be found by integrating (1.25) in time over the duration of the charge and discharge period $T = 1/f_{act}$, with f_{act} being actuation frequency.

  $$\overline{P} = \frac{1}{T}\int_0^T V(t)\, I(t)\, dt \tag{1.26}$$

  However, obtaining instantaneous values is not always straightforward. As for the voltage, its values can be easily measured either directly from the power supply or by means of high-frequency response probes for high voltage, and subsequently acquired through an oscilloscope or a data acquisition system. The situation is more complex for the discharge current: the measurement is carried out using a Rogowski coil connected in series between the ground and the grounded electrode. Since $I(t)$, due to micro-discharges, is characterized by very high frequencies and sudden peaks, probes with extremely high frequency response would be required. For this reason, the measurements are often imprecise and unreliable, and alternative techniques based on the time-integration of the current are usually preferred [10].

- **Electric charge method**
  The second method proposed by [10] makes use of a shunt capacitor with a known capacitance C_p connected in series between the grounded electrode and the ground. As the current flows through the capacitor, an electric charge accumulates on its plates, according to the relation:

$$Q_M(t) = C_p\, V_M(t) \tag{1.27}$$

  where $Q_M(t)$ is the instantaneous accumulated charge and $V_M(t)$ is the voltage across the leads. The current flowing through the capacitor is given by the time derivative of the charge on its plates:

$$I_M(t) = \frac{dQ_M(t)}{dt} = C_p\, \frac{dV_M(t)}{dt} \tag{1.28}$$

  and knowing that $I_M(t)$ is the same as the current flowing between electrodes $I_a(t)$, equation (1.25) can be rewritten as:

$$P_a(t) = V_a(t) \cdot I_a(t) = V_a(t) \cdot C_p\, \frac{dV_M(t)}{dt} \tag{1.29}$$

  This expression is already suitable for calculating instantaneous values of power consumption, however, to find the average power consumption, (1.29) can be rearranged and integrated over one cycle of actuation:

$$\overline{P_a} = \frac{1}{T} \int_0^T V_a(t)\, C_p\, \frac{dV_M(t)}{dt}\, dt \tag{1.30}$$

  and then:

$$\overline{P}_a = \frac{1}{T} \int_0^T V_a(t)\, C_p\, \frac{dV_M(t)}{dt}\, dt = \frac{1}{T} \int_0^T V_a\, C_p\, dV_M = \frac{1}{T} \oint_{\text{one cycle}} V_a\, dQ_M \tag{1.31}$$

  From formulas (1.30) and (1.31), two different approaches to evaluate $\overline{P_a}$ can be identified. The first consists in computing the integral of the time derivative of the voltage V_m. However, this quantity must be averaged over a sufficiently large number of cycles and carefully filtered.
  A second method relies on analyzing the behavior of the charge on the capacitor as a function of the voltage V_m, thus obtaining the so-called Lissajous curve. It is evident from equation (1.31) that $\overline{P_a}$ corresponds to the integral, over one charging and discharging cycle, of the obtained curve. Nevertheless, also in this case, appropriate filtering techniques must be applied in order to accurately extract the area.

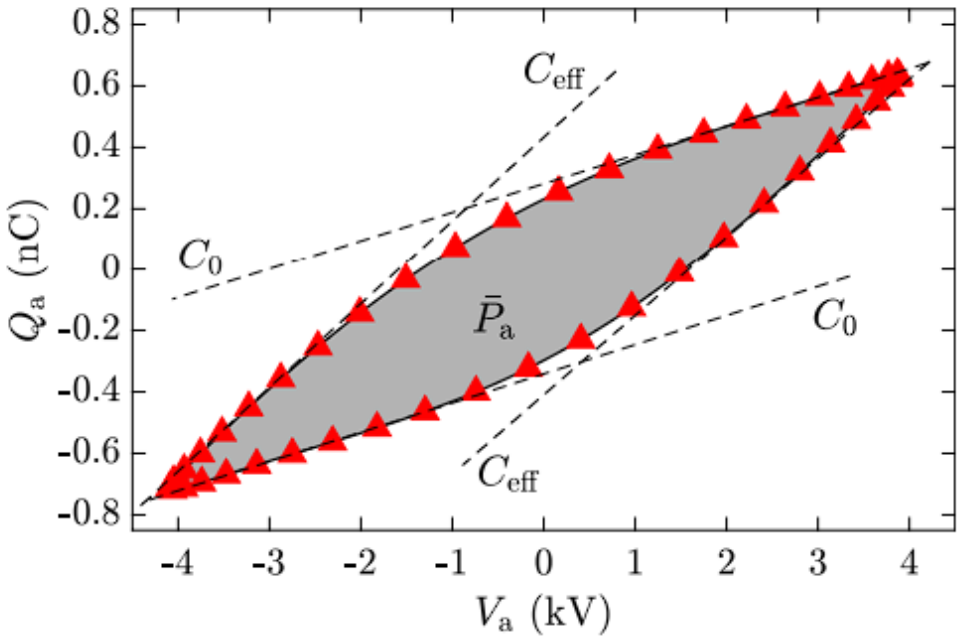

Figure 1.10: Typical Lissajous curve of voltage–charge for an AC-DBD actuator, focus on the slopes of the curve and its characteristic capacitances: C_0 and C_{eff}; reproduced from [11]

Important informations can be extracted from the Lissajous curve (Figure 1.10) by measuring its slope in different segments: cold capacitance C_0 and effective capacitance C_{eff}. C_0 is device-specific and, therefore, independent of the applied operating parameters, such as peak-to-peak voltage or actuation frequency; the effective capacitance C_{eff}, in contrast, determines the magnitude of the connected load and occurs during plasma formation.

Another critical aspect for correctly measuring the Lissajous curve is the choice of a capacitor with an appropriate capacitance. In fact, the equivalent capacitance can be obtained by considering two capacitors in series:

$$\frac{1}{C_{tot}} = \frac{1}{C_a} + \frac{1}{C_p} \tag{1.32}$$

It is clear that choosing a capacitance C_p that is too small strongly affects the circuit, excessively altering its electrical properties. On the other hand, selecting a capacitance that is too large (leaving the circuit characteristics unchanged) is not optimal either, as it would result in a signal with a very

low signal-to-noise ratio, requiring additional filtering and thus nullifying the advantage of this power measurement method.

To determine a suitable capacitance to be inserted, it is useful to plot the absorbed power P_a as a function of the capacitance itself, and then select a value within the constant portion of the resulting curve [12] (see Figure 1.11).

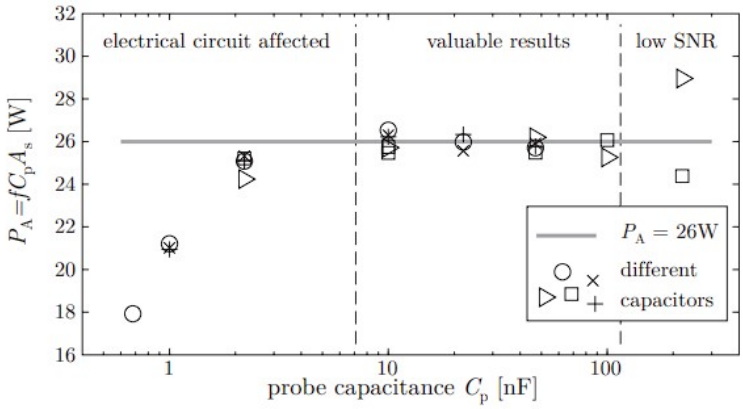

Figure 1.11: Expected results from the indipendency check of the probe capacitance; reproduced from [12]

1.6 Plasma based control of skin-friction drag

Given the popularity that plasma actuators have gained in recent years, owing to their numerous advantages, it is natural that research efforts are increasingly focused on them. Since the early 2000s, a wide variety of actuator configurations have been proposed, differing in actuation parameters, electrode geometry, and the type of flow in which they are implemented, ultimately leading to diverse outcomes. Although the theoretical effectiveness of plasma actuators is well established, in practice the results obtained have sometimes been contradictory. Therefore, it is crucial to continue both numerical simulations and experimental investigations in order to deepen our understanding of this highly promising technology. The aim of this section is to present the most relevant studies on active flow control using DBD plasma actuators for viscous drag reduction and to highlight the obtained results.

1.6.1 Jukes et al. 2006

One of the first and most known experiments on DBD plasma actuators operating in oscillating wall mode was carried out in 2006 by Jukes et al.[13]. The main objective of this study was to understand and optimize the geometric and modulation parameters of the actuator in order to achieve maximum drag reduction and to investigate the interaction mechanisms of the wall jet with the turbulent structures, evaluating the resulting variation in drag and turbulent kinetic energy. The studied flow is a turbulent boundary layer fully developed over a flat plate, placed inside a low-speed wind tunnel. In particular, the flow velocity is $U_\infty = 1.8$ m/s, with a $Re_\tau = 380$. The array configuration is presented in Figure 1.12. Measurements were conducted using Hot Wire Anemometry (HWA), with the probe placed between the exposed electrodes, at the dashed line in Figure 1.12.

The obtained results show that the plasma generates a meaningful velocity deficit in the boundary layer, especially in the logarithmic and buffer layers (Figure 1.13). This deficit is related to the formation of streamwise vortices and it grows with increased oscillation frequency:

$$T^+ = \frac{T u_\tau^2}{\nu}, \tag{1.33}$$

altering the near wall velocity gradient, thus reducing skin-friction drag. It should be noted that $T^+ = 12$ was the lowest achievable frequency with their equipment, suggesting that a further reduction in drag could be achieved with even lower T^+.

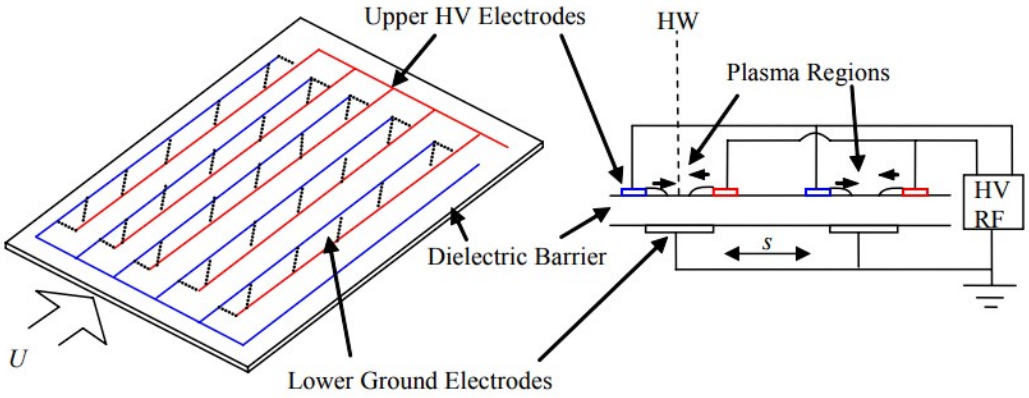

Figure 1.12: Configuration of Juke's arry of PAs. Two electrode sets are located on the exposed surface with a common bus between opposing pairs of electrodes. On the left: electrode sheet geometry. On the right: cross section through electrode sheet showing the location of plasma formation and direction of forcing; reproduced from [13].

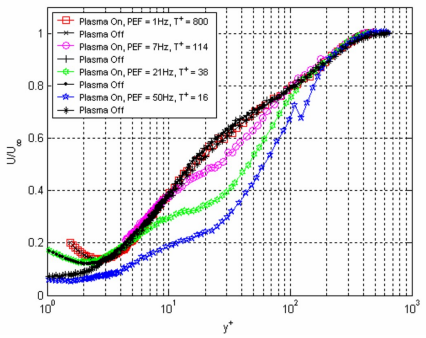

Figure 1.13: Mean velocity profile per different oscillation frequency T^+, scaled with canonical u_τ; reproduced from [13].

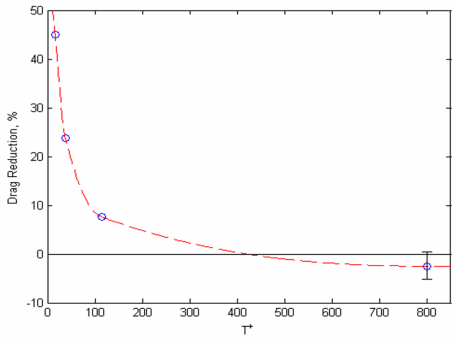

Figure 1.14: Variation of drag reduction with oscillation frequency; reproduced from [13].

With regard to the spacing between adjacent actuators S^+:

$$S^+ = \frac{S u_\tau}{\nu}, \tag{1.34}$$

this parameter has also proven to be crucial for achieving drag reduction. In fact, a decrease in drag is observed only at spacings on the order of 4 mm ($S^+ \approx 20$), as can be seen in the Figure 1.15.

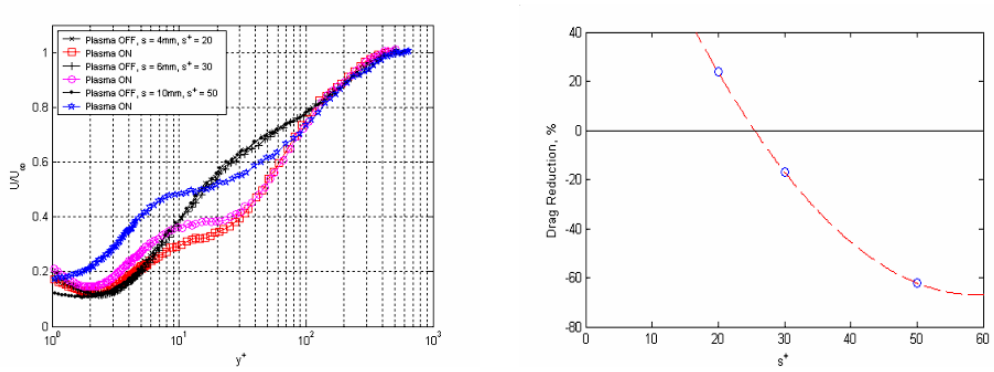

Figure 1.15: Influence of the spacing S. To the left: mean velocity profile with different electrode spacing. To the right: Variation of drag reduction with electrode spacing S^+; reproduced from [13].

The obtained result is likely due to the interaction of the vortices generated by adjacent electrodes, which must be sufficiently close to counteract the upwash and downwash motions. If this condition is not met, vertical velocity gradients at the wall may intensify, leading to an increase in drag. It is suggested that the plasma induced streamwise vortices are disrupting or cancelling the quasi-streamwise vortices (QSVs) which naturally occur near the wall, thus disrupting the whole turbulence regeneration cycle. This may be disrupting the link between the outer and inner boundary layer structures, so that these vortices act like a barrier to block large scale motions near the wall. An important consideration is that further reduction of the spacing was not feasible, since the plasma extension was approximately 3–4 mm; reducing S further would have resulted in arc formation between electrodes.
In the end, the best possible case resulted in a maximum drag reduction of 45% at $x^+ = 75$ downstream of the plasma actuators.

1.6.2 X.Q. Cheng et al. 2021

It is also possible to achieve drag reduction by operating the DBD plasma actuators in a continuous mode, thus following a "Large Eddy Break-Up" philosophy (LEBU), which aims to disrupt the coherence of large-scale turbulent structures (large eddies), responsible for a significant portion of the wall shear stress, by breaking up these large vortical motions into smaller, less energetic ones and ultimately reduce shear stress and friction drag.
A study about DBDs operating this way was conducted by X.Q. Cheng et al[14]. The experiment focused on testing three configurations of the actuators, which produced different spanwise arrays of large-scale streamwise vortices.

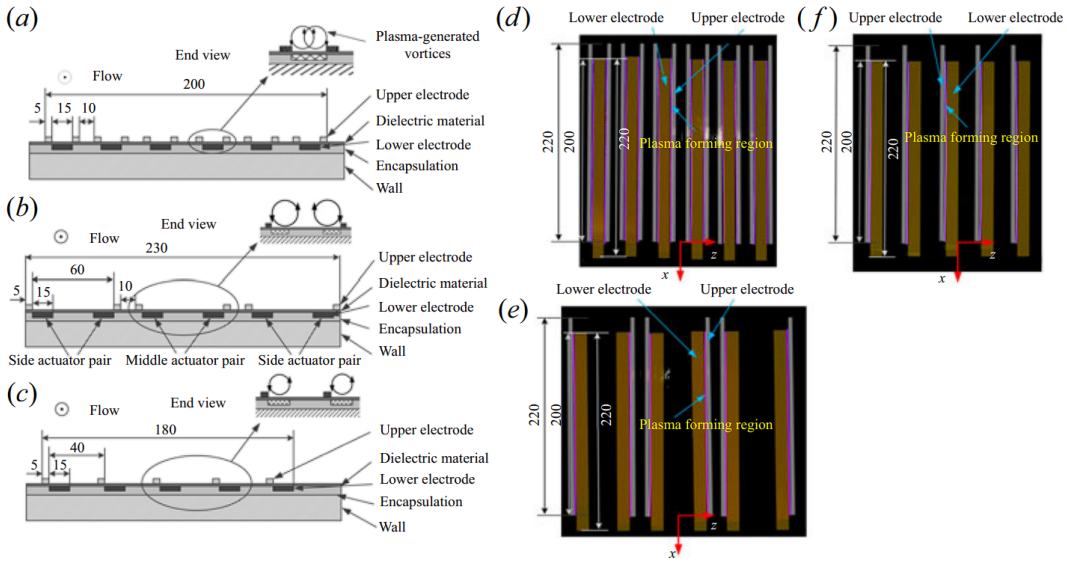

Figure 1.16: Schematic of three DBD plasma-actuator configurations (not to scale; dimensions in millimetres) and the photographs of the actuators and their discharges. (a,d) Configuration A ($S^+ = 100$), (b,e) configuration B ($S^+ = 400$), (c, f) configuration C ($S^+ = 267$). S^+ is the spacing between electrodes normalized with in wall dimensions; reproduced from [14].

In particular, it is possible to notice, from Figure 1.16, that configurations A and B generate counter-rotating Large-Scale Streamwise Vortices (LSSVs), while configuration C generates co-rotating LSSVs. The difference between A and B basically consists in the spacing between exposed electrodes: in fact, in configuration A, the produced LSSVs are close enough to interact with one-other, while in configuration B the adjacent electrodes are too far away from each other and the LSSVs don't interact.

Tests were carried out inside a wind tunnel that produced a mean flow of $U_\infty = 2.4$ m/s , with a $Re_\tau = 572$ and $u_\tau = 0.105$ m/s; while measurements were taken using hot-wire, PIV and a developed in house force balance for direct skin-friction measurements.

It was found that configuration B always outperforms A since the collision between vortices in A forms a strong upwash motion between the vortices generated by one actuator but a downwash one between adjacent actuators. Moreover this collision tends to lift up and weaken the vortices as they move downstream because of mutual induction, decreasing the effects of the actuator as the length of the electrodes increases. The drag reduction (DR) of configuration C is always less than that of A or B. The maximum DR is only 10% for configuration C, but

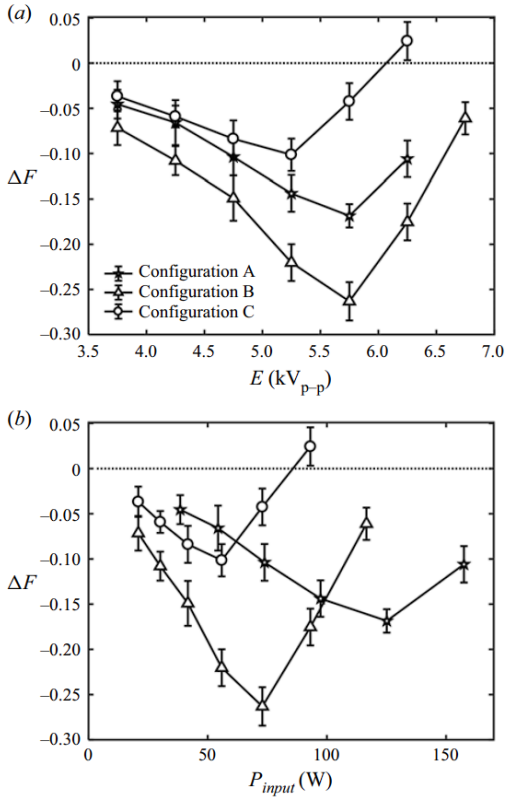

Figure 1.17: (a) Drag reduction, defined as $\Delta F = (F_{\text{on}} - F_{\text{off}})/F_{\text{off}}$, for configurations A, B, and C, where F_{on} and F_{off} are the floating-element-balance-measured skin-friction drag with and without the plasma actuator operated, respectively. (b) Variation of ΔF with the power input for the three plasma-actuator configurations; reproduced from [14].

approximately 20% and 26% for A and B, respectively, and it occurs at a peak to peak voltage $V_{pp} = 5.75kV$, beyond which the drag recovers rapidly (1.17). In fact, spanwise wall jet suppresses the random turbulent shear stress associated with the quasi streamwise vortices in the turbulent boundary layer, but above a certain level of the V_{pp}, vortices grow rapidly, and the coherent shear stress may exceed the reduction of the random shear stress, leading to a rise in drag.

For configuration B, it was also found that the drag reduction was not uniform in either the spanwise or the streamwise direction. Indeed, the spanwise distribution of $\Delta\tau_w = [(\tau_w)_{\text{on}} - (\tau_w)_{\text{off}}]/(\tau_w)_{\text{off}}$ revealed significant non-uniformity.

In Figure 1.18 (a) three regions can be clearly identified: the drag increase region (R1), the pronounced DR region (R2) and the drag recovery region (R3); while in Figure 1.18 (b), it is clear that the drag recovery is rather rapid from $x^+ = 0$ to 333 and is approximately linear further downstream until recovery at $x^+ \approx 2000$.

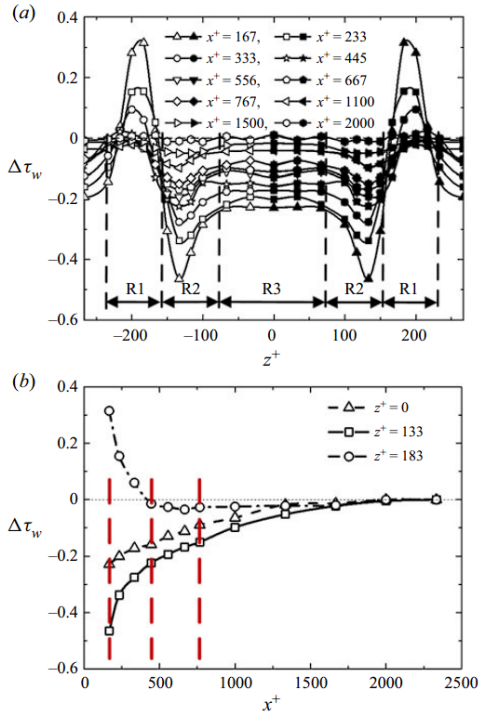

Figure 1.18: (a) Spanwise distributions of the local drag reduction = $\Delta\tau_w$. (b) Streamwise distributions of $\Delta\tau_w$.The red vertical dashed lines denote the locations of the PIV measurement Planes; reproduced from [14].

The change in the flow structure confirms that streaks are stabilized by the LSSVs, implying a drop in the generation of new QSVs (see Figure 1.19).

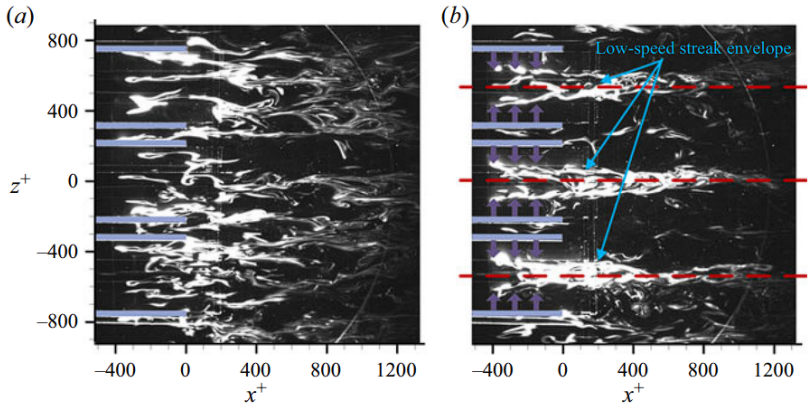

Figure 1.19: Smoke-wire flow visualization of instantaneous flow structure in the x–z planes. (a) Uncontrolled; (b) under control; reproduced from [14].

1.6.3 Zhi SU et al.2022

An experiment that directly compares different operating modes of the DBD plasma actuators was conducted in 2022 by Zhi SU et al.[15]. In fact, three different modes were tested: (a) unidirectional plasma jet, (b) impinging plasma jet, and (c) alternating oscillatory plasma jet. The actuator were then placed on a NACA 0012 airfoil at an angle of attack of 0° for wake evaluation and drag reduction calculation. The chord of the airfoil is 0.15m.

The experiments were carried out inside a close loop wind tunnel with free stream velocity of $U_\infty = 5$ m/s and 20m/s , with a $Re_c = 49700$ and 198000 respectively, while measurements were taken initially using a PIV setup, and then using hot wire, a Pitot tube and 16 pressure probes for the wake measuring system.

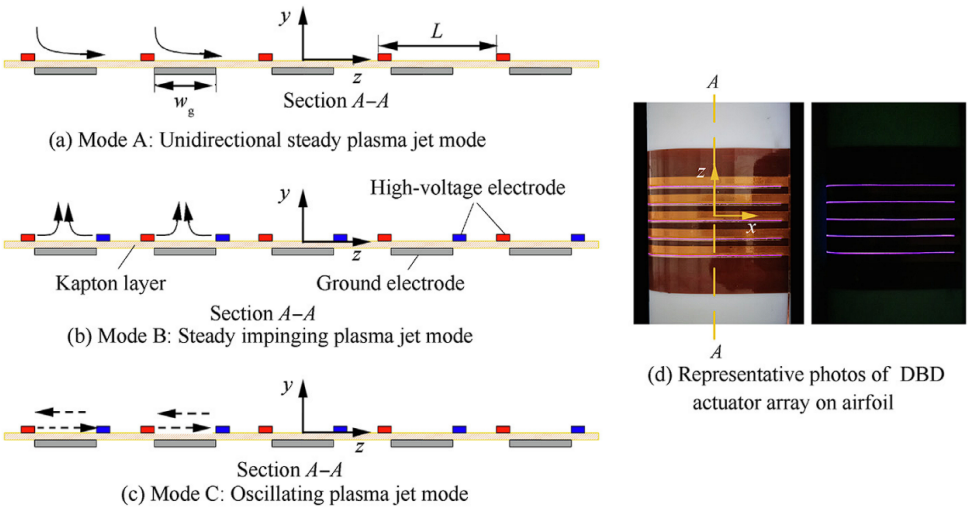

Figure 1.20: Configuration of the DBD plasma actuator array and the three operating modes; reproduced from [15].

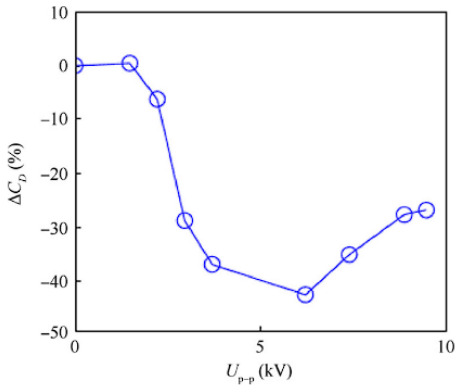

Figure 1.21: Variation of total drag with increasing voltage amplitude at $U_\infty = 5$ m/s. Reproduced from [15]

.

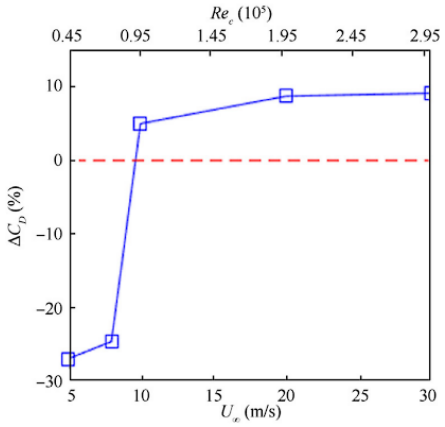

Figure 1.22: Variation of drag coefficient and drag reduction percentage with increasing freestream velocity at a fixed voltage amplitude. Reproduced from [15]

From wake measurements it is obvious that in all operating modes the peak velocity defect is reduced noticeably, but only two out of three modes yield an effective drag reduction effect, as can be seen in Figure 1.23, in particular mode A was found to be the best. Given the effectiveness of mode A on drag reduction, all subsequent tests were performed operating the DBDs in this way.

Therefore, an operating sweet spot was identified where the drag reduction (DR) reaches its maximum value when the peak-to-peak voltage is $V_{pp} = 6.2$ kV, while it was observed that, for a fixed V_{pp}, the DR decreases with increasing free-stream velocity, leading to a drag increase for $V_\infty > 10$ m/s(see Figure 1.21 and 1.22).

At last the influence of spanwise actuator spacing on drag reduction was studied. Three levels of L = 7, 10, 18 mm were realized, and the result shows that favorable drag reduction can only be achieved at low freestream velocity. The best performance was observed at L = 7 mm, $V_{pp} = 6$ kV and $V_\infty = 5$m/s, reaching a DR as high as 64%.

It is nevertheless interesting to note that drag reduction is achieved for all values of S^+ below 540 (Figure 1.24).

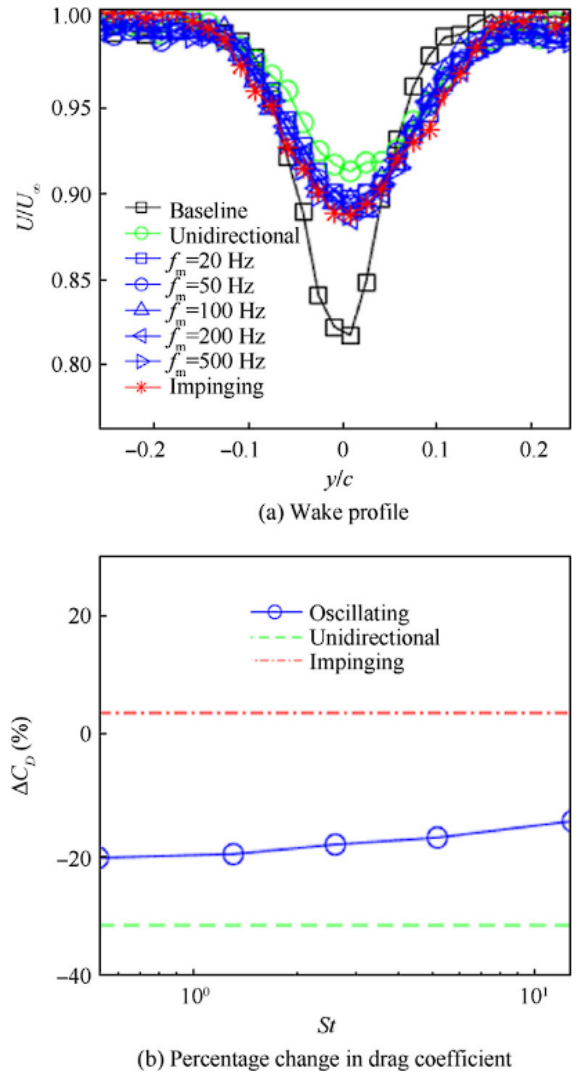

Figure 1.23: (a) Wake profile and (b) percentage change in drag coefficient at different working modes ($St = f_m c/U_\infty$, where c is the chord of the airfoil and f_m is the modulation frequency); reproduced from [15].

1.6.4 Benard et al.2024

An alternative way to shape the electrodes of a DBD plasma actuator was proposed by Benard et al. in 2024 [16]. The purpose of their research was to assess the effects of a wall-parallel standing wave, which means that the oscillations in the flow field were not obtained by modulating the generation of plasma in time, but by shaping the plasma itself in a sinusoidal waveform in space. In fact, the unique design of the

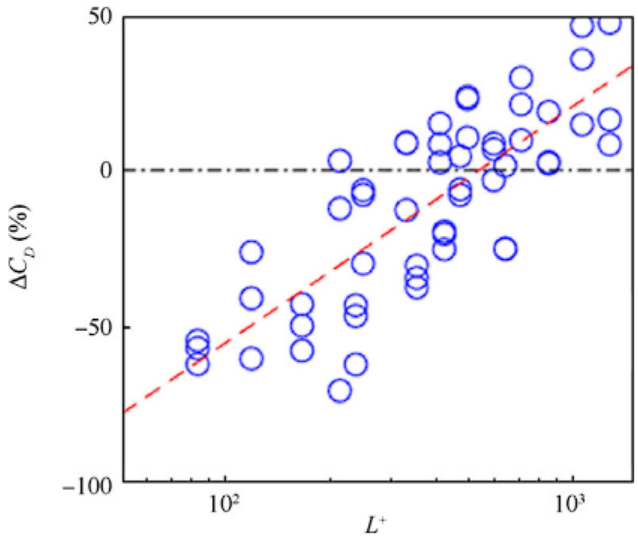

Figure 1.24: Scaling between drag reduction magnitude and dimensionless spacing; reproduced from [15].

electrode imposes constraints that force the flow to undergo periodic oscillations in space along the streamwise direction. The configuration of the actuators array can be seen in Figure 1.25. The geometric properties of the sinusoidal waveform are shown in table 1.1.

λ_x^+	A^+	S^+
1035	287	575

Table 1.1: geometric properties of the sinusoidal waveform. λ_x^+ is the straemwise wavelength normalized with wall parameters, A^+ is the amplitude of the sine wave normalized with wall parameters

Subsequently, wake measurements were carried out using a series of calibrated hot-films, along with planar PIV measurements parallel to the wall, in order to evaluate the generated drag reduction over a flat plate. The free stream velocity of the wind tunnel was set at $U_\infty = 10$ m/s, obtaining a local wall velocity $u_\tau = 0.43$ with the corresponding Reynolds number $Re_\tau = 370$.

The results obtained through hot films show both a decrease and an increase in drag depending on the amplitude of the high-voltage signal; in particular, for low voltages, a reduction in drag was achieved, while higher voltages led to an

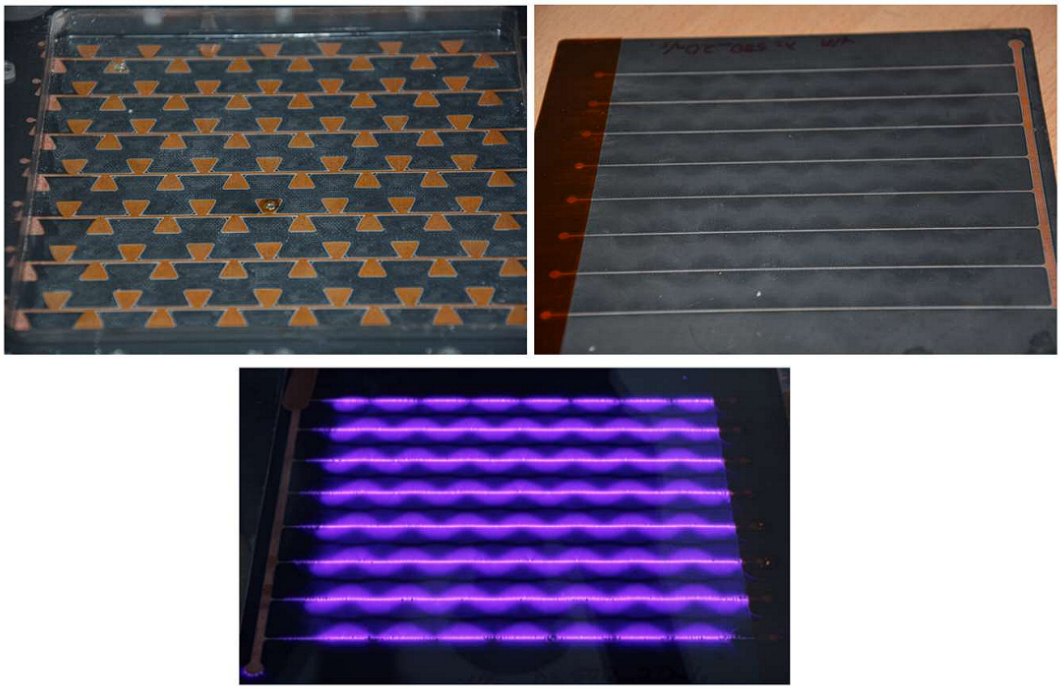

Figure 1.25: configuration of the DBD plasma actuator. Top left: encapsulated electrodes; top right: exposed electrodes; bottom: resulting sinusoidal plasma shape; reproduced from [16].

increase in local velocity u_τ and an overall increase in drag. Moreover, the higher the actuating frequency, the lower the voltage needed to be in order to have a beneficial effect on drag (see Figure 1.26).

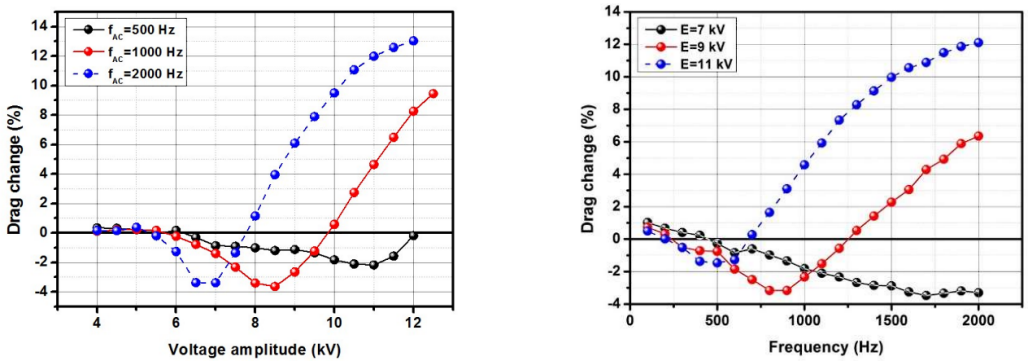

Figure 1.26: Total drag change for different voltage amplitude (left) and AC frequency (right); reproduced from [16].

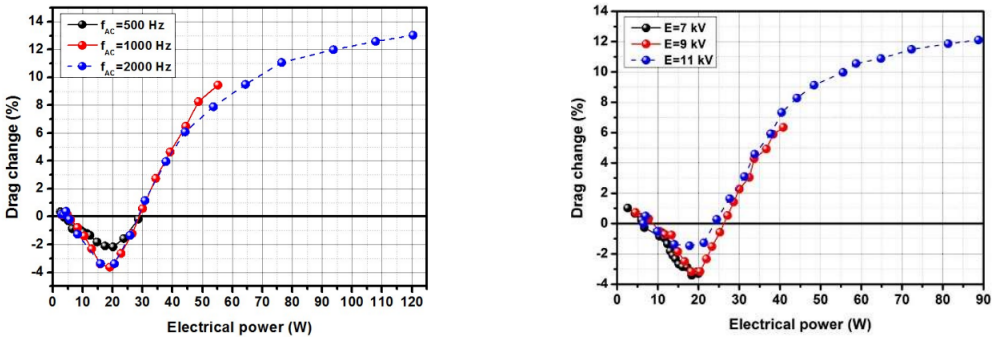

Figure 1.27: Effect of injected electrical power on total drag change; reproduced from [16].

The effects on overall power consumption were also considered and when the achieved drag modification was plotted against the consumed electrical power, all the results converged on a single curve, as can be seen in Figure 1.27. The maximum recorded drag reduction was only approximately of -4%, which may seem low at first, but what needs to be considered is that the hot film used for measurements was located at $x^+ = 1000$ downstream of the forcing region. Indeed the reduction in drag reduction diminishes rapidly with the streamwise distance downstream of the actuation endpoint ([17]). So, a length of two δ is sufficient to observe a 90% reduction in the observed drag reduction. If that was the case, directly over the electrodes, it was possible that this value could reach even -40%.

In order to validate this result, a PIV campaign was also performed. For the experiment it was chosen to illuminate with the laser blade a portion of the flow parallel to the wall, inside the buffer sublayer of the TBL (30-40 wall units above the surface). From Figure 1.28, it can be clearly observed that the flow was modified and the turbulent structures were reorganized. As the applied voltage increased, the high-speed streaks became wider in the spanwise direction, while the low-speed streaks tended to become narrower and more fragmented. This behavior may be attributed to the fact that higher voltages induce a stronger wall-normal velocity component, possibly leading to a reinforcement of ejection events.

Although, due to the laser positioning, it was not possible to effectively resolve the near-wall structures, it was nevertheless possible to compute the Reynolds stresses within the buffer layer. The results show that, as suggested by the hot-film measurements, only a moderate forcing leads to drag reduction, as evidenced by a mean reduction of the Reynolds stress tensor components compared to the uncontrolled case. Moreover, this effect occurs only within a specific region of the flow; moving downstream, an increase in the velocity magnitude is still observed.

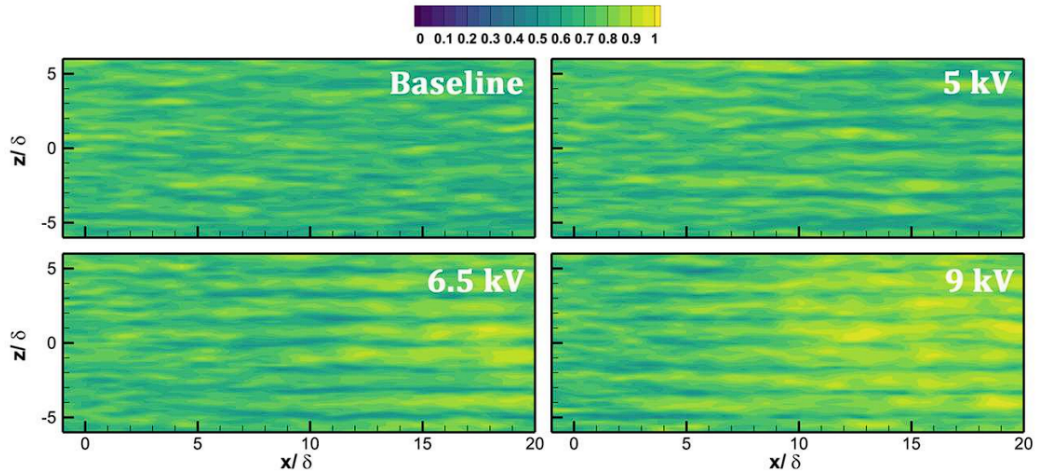

Figure 1.28: Snapshots of streamwise instantaneous velocity across a wall-parallel plane for 3 different forcing conditions; reproduced from [16].

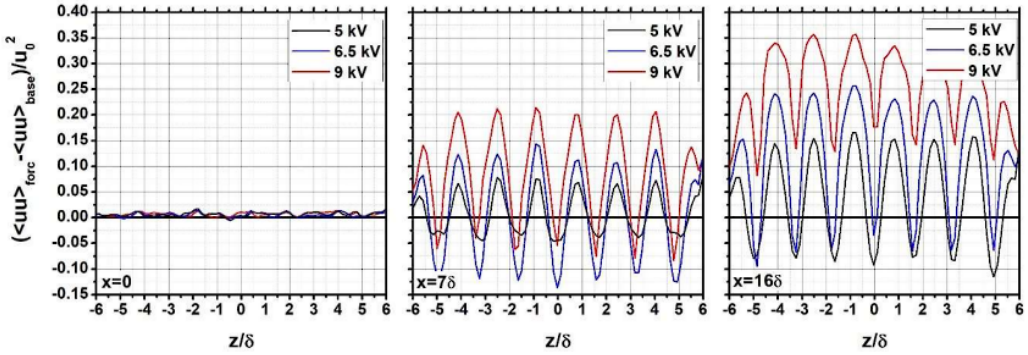

Figure 1.29: Spatial distribution along the spanwise of the field of view of the Reynolds stress component $< uu >$ compared to the value of the base flow; reproduced from [16].

1.6.5 Summary of the experiments

Table 1.2 highlights the differences and results obtained from all the experiments presented above. In designing the actuators for the present study, several of the factors reported here were taken into account. Their design and fabrication process will be discussed in greater detail in Chapter 2.

.

	best configuration	U_∞ **[m/s]**	u_τ **[m/s]**	S^+	**DR**
Jukes	oscillating wall	1.8	0.075	20	45%
Cheng	impinging jets	2.4	0.105	400	26%
Zhi SU	mono-directional	5 - 20	/	80	64%
Benard	standing wave	10	0.43	575*	4%

Table 1.2: Parameters and performance of different actuators, (*: see 1.1 for other geometrical parameters used).

1.7 Statement of work

Although DBD plasma actuators have been extensively studied in recent years due to the many advantages they can offer in terms of flow control and drag reduction, as well as their relative simplicity of construction, the vast majority of the work carried out so far has not departed significantly from the "traditional" configuration with linear electrodes. However, as in the example by Benard et al. discussed in Section 1.6.4, it is possible to design actuators with different geometries while still achieving positive and satisfactory results in terms of drag reduction [16].

Following Benard et al. approach, the goal of this thesis is to deepen the understanding of a non-conventional actuator configuration and to design and manufacture an array of actuators with sinusoidally shaped electrodes, which is then electrically and mechanically characterized, in terms of consumed power and body force produced. Due to the broad range of topics addressed, the thesis naturally assumes a dual character, with some chapters dedicated to electrical measurements and others focusing instead on the mechanical characterization.

It is important to add that the new actuators introduce several innovations compared to those previously developed at Politecnico di Torino, as they make use of brush-applied nickel-based conductive paint which is then applied on a stencil obtained with a laser pantograph. This allows for a faster and more reproducible manufacturing process, even for larger scale actuators. Finally, it was necessary to explore the use of new materials, such as polystyrene sheets employed as dielectrics, and epoxy resin used as insulating material.

To conclude, this work also aims to lay the foundations for possible future drag measurements inside a boundary-layer wind tunnel in the presence of flow, in order to assess the actual influence of plasma on the velocity field of a turbulent boundary layer. In addition, it provides useful information for the future manufacture of new actuators of various shapes and sizes.

Chapter 2

Methodology

The objective of this chapter is to illustrate the development, manufacturing, and measurement processes carried out throughout this thesis project. The equipment, components, and experimental setup used during each phase of the work will be presented, together with the operations performed and the rationale behind the design choices that were made.

2.1 DBD actuators design

2.1.1 Geometry

The main idea behind this project was to design an array of actuators with a different geometry from the usual one with straight electrodes: following the lead of Benard et al. ([16]) an actuator composed of sinusoidal electrodes was built, as to reproduce the effects of a standing-wave. In order to avoid arbitrarily defining the geometric characteristics (such as the spacing between exposed electrodes, wavelength and amplitude of the sinusoidal wave), the design was guided by previous studies, in particular those conducted by Jukes et al.[13], Benard et al.[16], Henher et al.[4], and Cheng et al.[14]. The geometric parameters used in their work, normalized with the traditional friction velocity u_τ, were taken as reference and subsequently scaled to match the conditions of our wind tunnel, which is an open-circuit boundary-layer model (Figure 2.1).

In order to normalize the dimensions of the actuators array it was necessary to know the value of u_τ inside the wind tunnel. The floor of the test section consists of a flat plate, on which, 3.5 m downstream from the leading edge, the location for installing the plasma actuators is positioned. Knowing the kinematic viscosity $\nu = 1.55 \times 10^{-5}$ m^2/s and assuming a free-stream velocity of $U_\infty = 15$ m/s, it is

Figure 2.1: boundary layer wind tunnel of Laboratory of Aeronautics M. Panetti of Politecnico di Torino.

possible to compute the local Reynolds number at the actuator location. From Re_x, it is possible to determine the value of the skin-friction coefficient C_f using the semi-empirical correlation valid for a turbulent boundary layer over a flat plate:

$$C_f = \frac{0.0576}{Re_x^{1/5}} \tag{2.1}$$

The exact value of C_f had also been experimentally measured prior to the beginning of this thesis work, and the obtained value is in agreement with that predicted by these empirical correlations. Finally, u_τ can be calculated as:

$$u_\tau = \sqrt{\frac{1}{2} C_f U_\infty^2} = 0.566 \text{ m/s} \tag{2.2}$$

Based on this value, the main geometric parameters were scaled from the dimensions used by Bénard et al.[16] in their experiment. The resulting actuator configuration was finally designed: a 26 x 26 cm^2 array of 12 exposed sinusoidal shaped electrodes. It should be noted that, our electrodes are actually sinusoidal shaped, while, in the before mentioned experiment, only the plasma assumed a wave-like shape, even if the electrodes themselves were not sinusoidal. The parameters used are the following

- **spacing** S of 15.7 mm ($S^+ = 575$) between exposed electrodes;

- **semi-amplitude** of the sine wave A of 7.85 mm ($A^+ = 287.5$);
- **streamwise wavelength** λ_x of 28.3 mm ($\lambda_x^+ = 1035$)
- **electrodes width** of 2 mm.

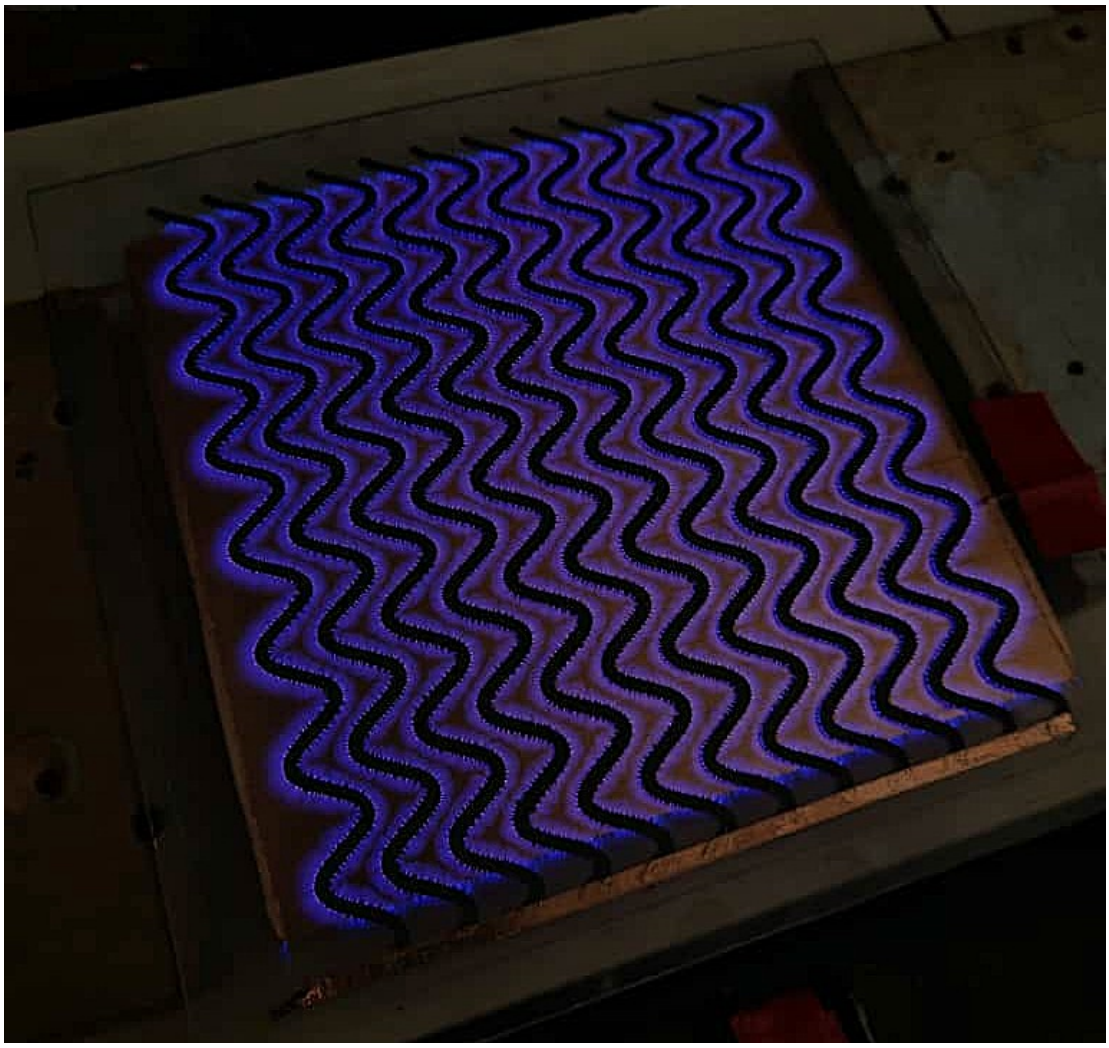

Figure 2.2: Picture of the DBD plasma actuator array and its discharge.

2.1.2 Fabrication

To manufacture actuators with complex geometries (described in chapter 2.1.1) and to improve fabrication accuracy, a black adhesive stencil cut by a laser pantograph was employed. The geometry itself was designed using CAD software.

Subsequently,the feasibility of construction with several materials was evaluated and tested, including 0.5 mm thick PET sheets as dielectric material, and graphite- or silver-based conductive paints for the electrodes. The PET sheets, unfortunately, were too thin for such a large array and, due to the heat generated during operation, the material tended to bend excessively, which led to changes in the electrical characteristics of the system and, more critically, to the detachment of the insulating layer and premature dielectric breakdown. If the array was to bend excessively, it would also be a problem for the acquisition of PIV images and, eventually, when placed in the wind tunnel in the presence of air flow. The best results were finally obtained using a 2 mm thick transparent polystyrene sheet as dielectric (which can withstand voltages up to 50 kV before dielectric breakdown occurs), combined with nickel-based conductive paint for the electrodes. The polystyrene sheet resulted in a much sturdier and more rigid actuator, even if some bending still occurred when it was operated for an extended period of time at high input voltage. The entire encapsulated side was fabricated by applying a continuous layer of copper tape which was then insulated by four layers of 50 μm thick Kapton tape.

2.2 Electrical characterization

2.2.1 Equipment

To perform the electrical characterization of the actuators, appropriate instrumentation is required:

- A **DC power supply** (*Voltcraft VSP 2410*) is used to provide the necessary electrical power to the system.
- The signal, in the form of a square wave, is generated by a **function generator** (*RS Pro AFG-210005*) and must be amplified from a few volts up to several kilovolts.
- For this purpose, a *GBS Elektronik GmbH Minipuls 4* **high voltage source** is employed. It consists of a bridge converter that generates a low-voltage square wave, which is subsequently amplified through a cascade of transformers, reaching peak-to-peak voltages up to 40 kV in alternating current (sinusoidal waveform).
- To monitor in real time the high-voltage AC signal generated by the transformer cascade a digital **oscilloscope** is used (*RS-PRO RSDS 1102CML+*).

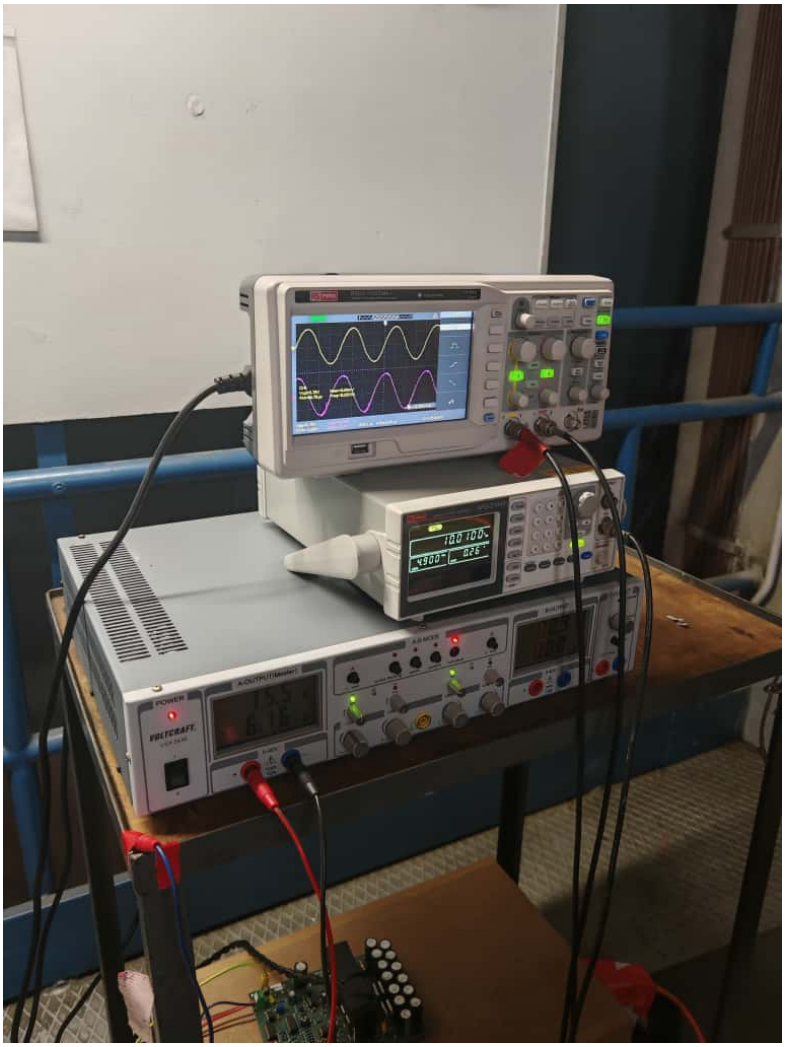

Figure 2.3: Equipment used to power and characterize the actuator. From top to bottom: oscilloscope, function generator, power supply.

In order to obtain a first estimate of the velocity induced by the actuators, a pressure transducer (*FCO560 Calibrator*, Figure 2.5) was used to measure the pressure difference between the ambient pressure and the pressure recorded in the vicinity of the exposed electrode generating the plasma. The measurements were taken with a small glass tube with an inner diameter of 1.1 mm. Using Bernoulli's relation, it is possible to estimate the induced velocity w_{induced}.

$$\Delta p = p_{\text{amb}} - p_{\text{meas}} = \frac{1}{2}\,\rho\, w_{\text{induced}}^2 \tag{2.3}$$

where p_{meas} is the pressure measured near the actuator. It should be noted

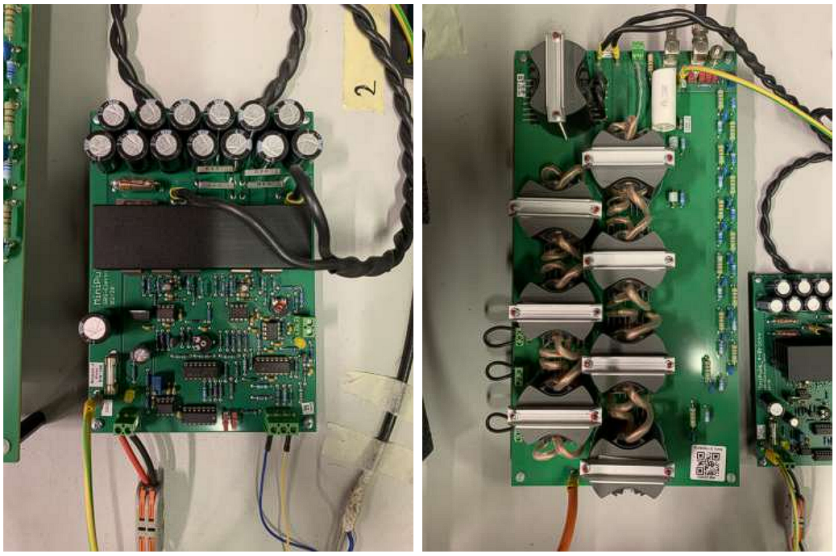

Figure 2.4: The two element of the *Minipuls 4*: on the left the bridge converter; on the right the transformer cascade.

that the measurements carried out in this manner have purely qualitative value, since many of the assumptions required for the correct application of Bernoulli's theorem are not fulfilled. For instance, the fluid cannot be considered to have constant density (as it is slightly heated by the plasma), the flow is not stationary, and viscous effects cannot be neglected. Moreover, the diameter of the probe used is excessively large for the type of measurement being performed, as the wall-jet generated by the actuator is extremely close to the surface. As a result, the probe risks to significantly alter the flow in its vicinity.

2.2.2 Selection of operative actuation frequency

The first step for the electrical characterization of the array of plasma actuators is to find a suitable actuation frequency to operate. The objective is to find at which frequency the induced velocity reaches the maximum value, but also avoid operating directly on top of the resonance frequency. The resonance conditions are determined by a combination of actuation frequency and applied voltage, and result in a sudden and substantial increase in the absorbed current, leading to a larger and stronger generation of plasma (although in filamentary form, which isn't the preferred form of plasma emission [7]), and potentially causing malfunctions or even damage to the instrumentation. The resonance condition is determined not only by the actuator, but is a property of the entire electrical system, including the power supply and the high voltage source.

Figure 2.5: Pressure transducer

Another aspect to keep in mind is that the instrumentation used has same safety limitation on maximum input current and input voltage, so it is necessary to operate the actuators below these limits:

- maximum current $I = 10\text{A}$
- maximum supplied voltage $V_{supply} = 35\text{V}$

In order to measure the performance and the power consumption of the array of DBD actuators as actuation frequency changes, the peak-to-peak voltage across the actuator was kept fixed at 14 kV. This value was chosen because, given our system and the limitations implied, it could be achieved for almost all actuation frequencies within the 5–12 kHz range. Both the current and the voltage supplied by the power supply were measured, together with the plasma-induced wall velocity at a distance of 4 mm from the exposed electrode. According to [18], this location corresponds to the point where the magnitude of the induced velocity reaches its maximum. The sampling frequency f_{samp} was set to 1.25 MHz, allowing the evaluation of the relevant quantities over a sufficient number of charge–discharge cycles while maintaining adequate resolution within a single cycle. Indeed, the number of samples N_{samp} is fixed at 10000, and therefore the acquisition time T_{acq} is given by:

$$T_{\text{acq}} = \frac{N_{samp}}{f_{\text{samp}}} \tag{2.4}$$

while the number of acquired cycles can be expressed as:

$$N_{\text{cycles}} = T_{\text{acq}} \cdot f_{\text{act}} \tag{2.5}$$

The capacitance of the shunt capacitor described in section 1.5.1 was initially chosen with a value of 235 nF. This value was chosen arbitrarily, with the awareness that it may yield inaccurate power measurements, but this is not relevant right now, as the real study of consumed power will be performed in a later step.

2.2.3 Selection of the shunt capacitor

Once a design operating frequency was determined, it was necessary to identify an appropriate capacitance for an accurate measurement of the power consumed by the actuators. To this end, it is required that the consumed power value remains approximately constant over a certain range of capacitances (see Section 1.5.1). Therefore, measurements were taken maintaining the most homogeneous operating conditions possible throughout this investigation (Table 2.1), and by varying the capacitance C from 1 nF to 5000 nF. For every capacitor, the area enclosed in the Lissajous curve and the corresponding average power consumption were computed.

f_{act} [kHz]	f_{samp} [MHZ]	V_{pp} [kV]	V_{supply} [V]
10.10	1.25	17.28	29

Table 2.1: Operating conditions during the investigation. V_{supply} is the peak to peak voltage measured on the actuator, while V_{supply} is the input voltage supplied by the power supply.

2.2.4 Consumed power

With an effective capacitance value finally selected, it was possible to measure the effective power consumed by the actuators when they are supplied with different input voltages - and corresponding peak-to-peak voltages. The operative conditions of these measurements are shown in table 2.2, while V_{supply} was ranging from 12 to 29 V. Another parameter that was computed, although subjective for our setup, is the electrical efficiency $E = P_{consumed}/P_{input}$, where $P_{input} = I_{input}V_{supply}$.

f_{act} [kHz]	f_{samp} [MSa]	C_{probe} [nF]
10.10	1.25	300

Table 2.2: Operating conditions during the investigation, measurements taken as a function of V_{supply} and V_{PP}

2.2.5 Variation of consumed power in time

The last analysis that was performed for the electrical characterization of the array of plasma actuators was to measure the variation of consumed power over the span of 3 minutes. Although the duration of the experiment is not long enough to draw definitive conclusion, the results can still be representative of the performance decay of the actuators during operation.

The operative conditions for this experiment are shown in table 2.3.

f_{act} [kHz]	f_{samp} [MSa]	V_{supply} [V]	C_{probe} [nF]	time duration [s]
10.10	1.25	29	300	180

Table 2.3: Operating conditions during the measurement.

Since any variation in consumed power is reflected on the shape of the Lissajous curve, the cold capacitance C_0 was also computed to check if any changes occurred to this parameter. In fact, some combinations of materials used for the dielectric and the electrodes are more prone to deterioration over time than others, resulting in a steady decline in C_0 [11].

2.3 PIV campaign

In order to perform a mechanical characterization of the actuators, it is necessary to obtain the mean flow field around the exposed electrodes. The most suitable method to achieve this is through acquisition of stereo PIV images. The equipment used for this purpose, as well as the measurements performed, are presented in the following sections.

2.3.1 Current setup

For our experiments, a Laskin nozzle was employed to generate the required seeding. This device operates by injecting high–pressure air (approximately 2 bar) into DEHS oil contained inside the seeder, allowing the liquid to atomize in particles of

approximately 1 μm and disperse into the measurement volume. A portion of this volume is illuminated by a high–power laser (a 200 mJ/pulse dual–cavity *Litron laser* operating at a maximum frequency of 15 Hz). The dual–cavity configuration enables the generation of two independent laser pulses, which can be emitted at very high frequency (on the order of MHz). These pulses correspond to the acquisition of two frames, A and B, which are subsequently cross–correlated in order to find the velocity field. After being emitted, the laser pulse passes through a system of lenses and mirrors whose purpose is to adjust it in the correct direction and shape it into a very thin sheet only a few millimeters thick. In particular, two mirrors, one cylindrical lens, and one spherical lens were employed to achieve the required characteristics. To capture these high–frequency images, two *Andor Zyla ZL41 sCMOS cameras* (5.5 Mpx, sensor size 2560 $\times$ 2160 pixels^2) were used. Each camera is equipped not only with a 100 mm fixed focal length lens with a 2x teleconverter, but also with a Scheimpflug adapter that allows the camera sensor plane to be tilted with respect to the optical axis in order to satisfy the Scheimpflug condition and to ensure that the entire illuminated plane remains in focus despite the oblique viewing angle. All of these components are mounted on a supporting structure capable of translating in the streamwise direction by means of a hand-wheel, allowing the acquisition of images at different measurement planes.

Figure 2.6: *Litron laser*

Figure 2.7: *Andor Zyla ZL41 sCMOS* camera

Figure 2.8 provides a schematic representation of the complete setup, highlighting the main components.

2.3.2 PIV measurements

Our sPIV setup is designed to capture images of a plane perpendicular to the wall, with a hypothetical wind–tunnel flow oriented orthogonally to it. The objective is

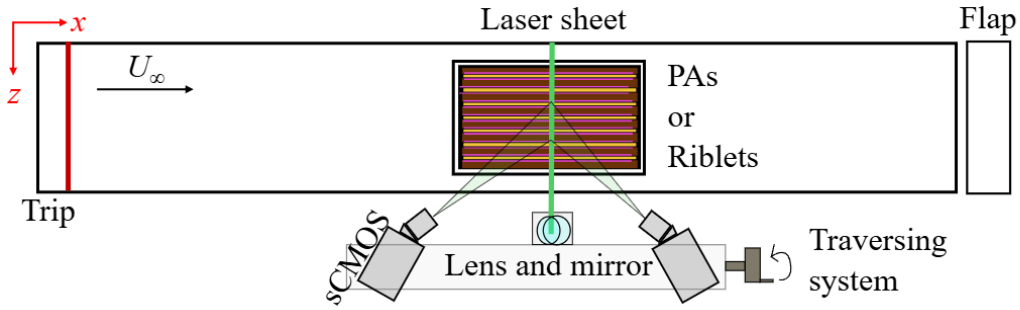

Figure 2.8: Schematic of the considered sPIV setup, showing the inside of the boundary layer wind tunnel where the array of actuators is placed.

therefore to perform cross–flow measurements, which are essential for resolving the three–dimensional structure of the near–wall flow, visualizing the vortical structures generated by the DBD plasma actuators, and ultimately assessing the variation of wall shear stress and the resulting drag–reduction effects. The array of sinusoidal actuators was installed inside the wind tunnel, placed within a hatch on the wall of the flat plate so that it remained as aligned to the surface as possible. Subsequently, under quiescent air conditions, that is, without any flow induced by the tunnel, the surrounding volume was seeded, thus enabling measurements useful for the mechanical characterization of the actuators, in particular the induced velocity and the generated thrust.

Velocity fields were measured in five different planes. The first three planes (A, B, C) intersect the electrodes in the spanwise direction, while the last two (D, E) were obtained by rotating the tile on which the actuators were mounted by 90°, basically aligning the laser along the streamwise direction. These measurement positions are shown in Figure 2.9 and correspond to:

- **Plane A:** Positive peak of the sinusoidal wave;
- **Plane B:** Intermediate plane between the maximum and minimum of the sinusoidal wave;
- **Plane C:** Negative peak of the sinusoidal wave;
- **Plane D:** Plane equally spaced between one electrode and its adjacent electrode;
- **Plane E:** Plane equally spaced between the maximum and minimum points of a single sinusoidal electrode.

For every plane, two sets of measurements were acquired at two different input voltages, 26 V and 29 V. Moreover, the images were acquired approximately

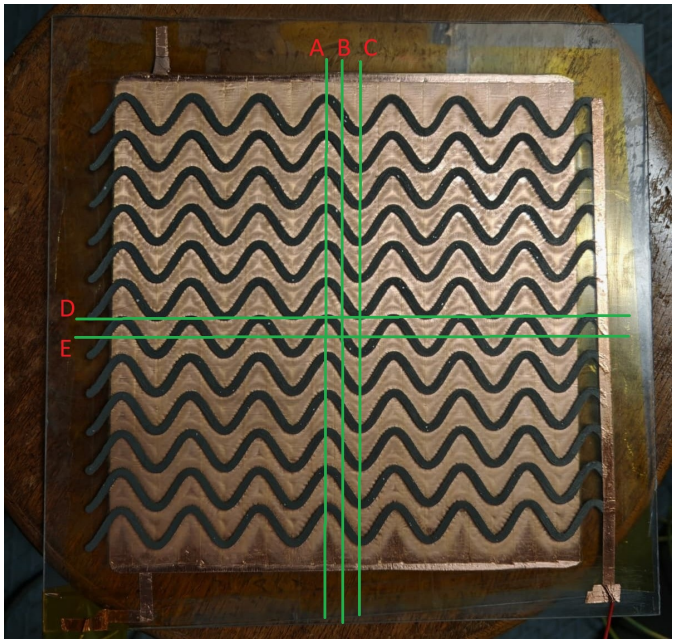

Figure 2.9: different planes of measurement

60 seconds after the actuator was switched on. This was done to approach, as closely as possible, the steady operating condition of both the actuator and the surrounding fluid. Additionally, as discussed in Chapter 2.1.2, although the material used (polystyrene sheets) proved to be stiffer than PET, it still exhibited slight bending due to heating produced by the Joule effect, locally raising the wall position in the PIV images. By allowing the actuator array to "warm up" for about one minute before acquiring the snapshots, the wall position, although slightly raised from the wall plane, remained approximately constant throughout the entire measurement duration. However this deformation lead to some of the domain to be less illuminated by the laser beam, especially at negative z values. Nonetheless at least 4 electrodes are present in every field of view and so these effects can be identified and eventually accounted for. This undesirable behavior posed not much of a problem for our current measurement in quiescent air, but might induce some errors in future drag reduction investigation within the wind tunnel when there is air flow.

The actuation parameters of the PAs used during measurements are reported in table 2.4.

V_{supply} [V]	f_{act} [kHz]
26–29	10.1

Table 2.4: Parameters used for operating the array of actuators during PIV measures.

The obtained velocity fields are averaged across approximately 900 snapshots acquired at a frequency of 15 Hz. The statistical convergence has been assessed by observing no significant change in the variables of interest.

Chapter 3

Results

3.1 Electrical characterization

3.1.1 Operative frequency

It is first important to check if the capacitor used for measurements has an acceptable capacitance value. Taking as an example the results obtained for $f_{\text{act}} = 10$ kHz, it was observed that the resulting Lissajous curve exhibits a rather regular shape (Figure 3.1). Furthermore, the frequency spectrum clearly shows that the energy is concentrated around the peak located at $f_{\text{act}} = 10$ kHz (Figure 3.2), meaning that the sampling frequency is high enough to acquire an adequate number of points over each charge and discharge cycle and to accurately resolve the actuation frequency.

The obtained results are shown in Figure 3.3, 3.4 and 3.5. As mentioned above, for all these measurements, V_{pp} was kept constant at 14kV, but in some cases this was not possible due to the safety limitation of the instrumentation (discussed in section 2.2.2) or simply because the power output was not high enough to reach the target V_{pp} voltage. The measurement points where this problem occurred are appropriately marked in the plots.

From Figure 3.3, it is clear that the resonance frequency is located between 8kHz and 9kHz since there is a spike in the input current. It is then necessary to avoid operating the DBDs in this range of frequencies. The supply voltage, on the other hand, shows an opposite trend with respect to the current. Within the resonance range, its value decreases considerably and then gradually increases again as the system moves away from resonance. The trend of the input power ($P_{input} = V_{supply} \cdot I_{input}$) is nearly linear with frequency. Figure 3.4 shows the effective power consumed by the actuator array and its electrical efficiency. The

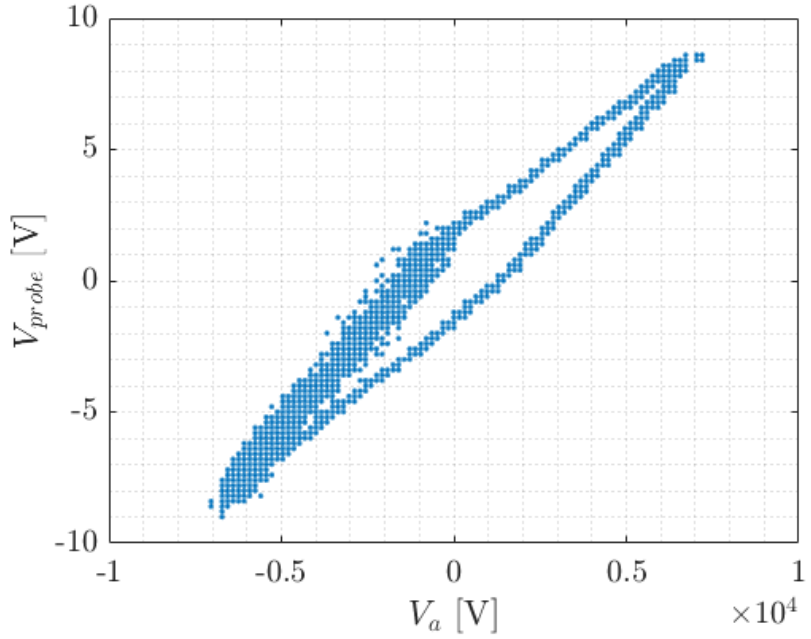

Figure 3.1: Example of obtained Lissajous curve.

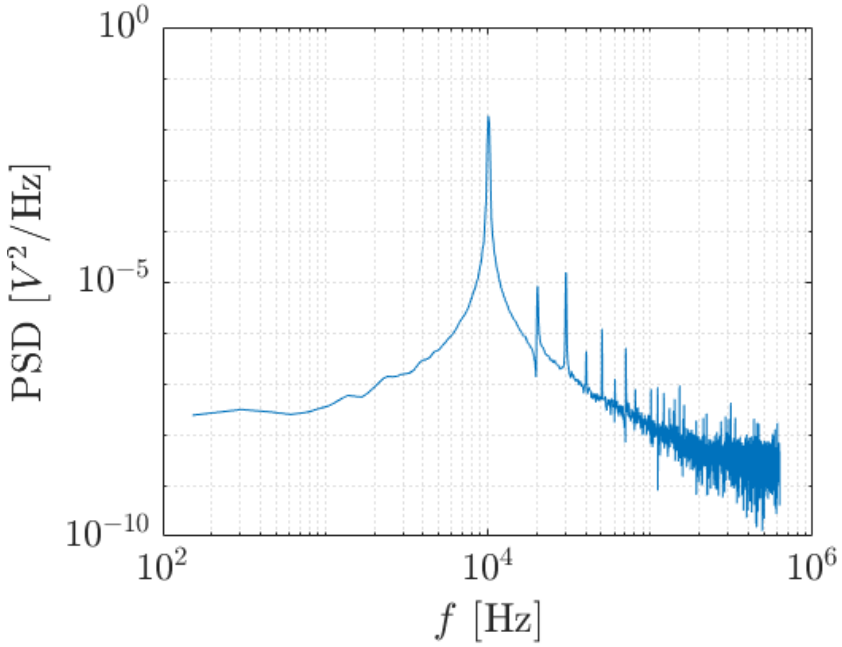

Figure 3.2: Power spectral density for $f_{\text{act}} = 10$ kHz.

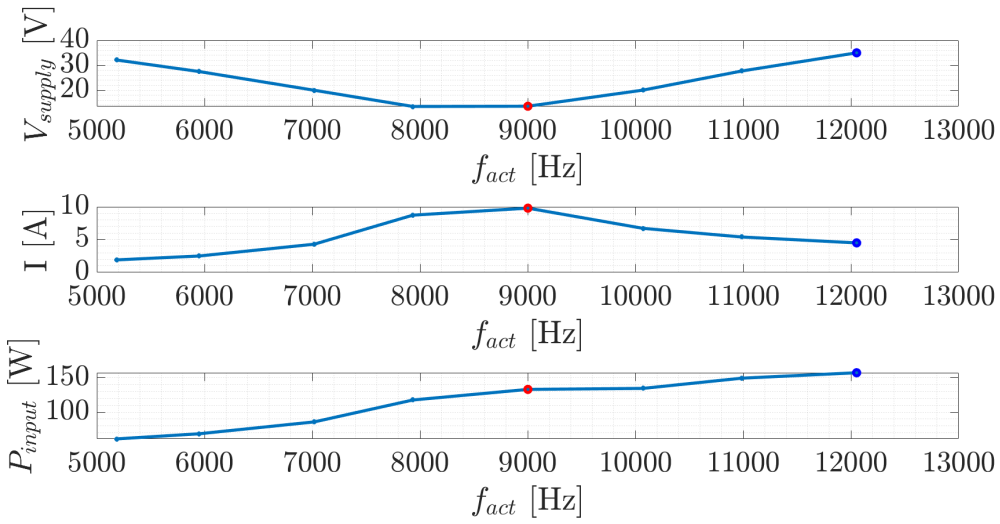

Figure 3.3: Plot of input electrical quantities as a function of the actuation frequency. From the top: voltage supplied V_{supply} [V], input current [A], input electrical power P_{input}[W]. (Red circle: $V_{pp} = 13.12$kV; blue circle: $V_{pp} = 13.2$kV, the other points are supplied at $V_{pp} = 14$kV).

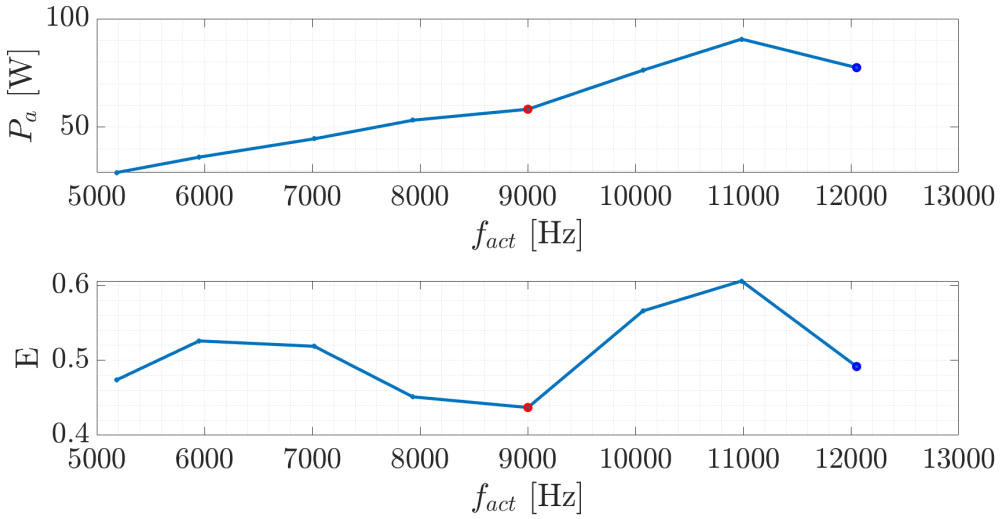

Figure 3.4: Plot of effective electrical power P_a consumed by the actuators and electrical efficiency E, defined as $E = P_a/P_{input}$. (Red circle: $V_{pp} = 13.12$ kV; blue circle: $V_{pp} = 13.2$ kV, the other points are supplied at $V_{pp} = 14$kV).

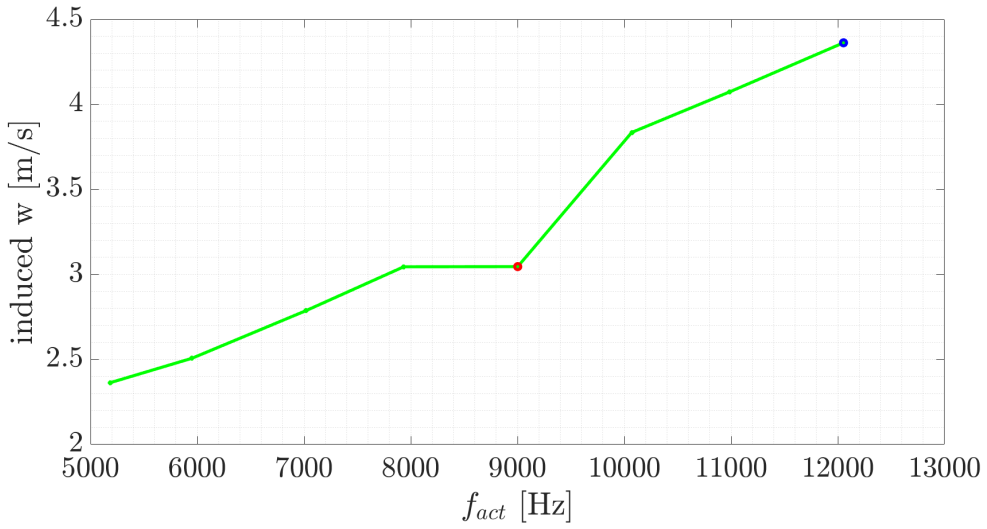

Figure 3.5: Variation of the induced velocity w with the actuation frequency f_{act}. (Red circle: $V_{pp} = 13.12$ kV; blue circle: $V_{pp} = 13.2$kV, the other points are supplied at $V_{pp} = 14$kV)

consumed power seems to have a linear behavior, similar to the input power, while E strongly decreases near the resonance frequency. Figure 3.5 shows that the induced velocity w reaches its maximum for $f_{act} = 12$ kHz. It should be noted, however, that all these measurements were carried out at a constant peak-to-peak voltage V_{pp} for all actuation frequencies. This voltage value was selected such that it could be achieved for almost all actuation frequencies within the 5–10 kHz range and thus adequately isolate the effects of this input parameter. For some frequencies, however, higher V_{pp} values can be reached by increasing the supply voltage without surpassing the safety limitations of the equipment, which lead to the highest observed induced velocity described in Table 3.1.

f_{act} [kHz]	V_{input} [V]	V_{pp} [kV]	I [A]	$w_{induced}$ **[m/s]**
10.10	29.00	17.28	8.06	4.92
12.00	35.00	13.92	4.50	4.36

Table 3.1: Operating conditions for maximum induced velocity

To summarize the process that led to selecting the applied tension and frequency: the resonance frequency was first identified by fixing a value of V_{pp} and observing how the absorbed power varied with the signal frequency. Simultaneously, the induced velocity was measured. The final operating parameters were chosen at a

frequency above resonance, where both the induced velocity and the actuator's electrical efficiency are high. This improved efficiency made it possible to further increase the supplied voltage, which in turn enhanced the induced velocity, as reported in Table 3.1. In light of the obtained results, it was decided to operate the actuator array at an actuation frequency of $f_{\text{act}} = 10.1$ kHz, since it is generally preferable to operate the actuators at frequencies slightly higher than the resonance frequency [19]. Moreover, it provided a good compromise between stability, induced velocity, and electrical efficiency.

3.1.2 Shunt capacitor

For small capacitance values, the resulting Lissajous curve exhibits an almost circular shape, which indicates a significant phase shift between the signal across the actuator and that across the shunt capacitor [19]. Moreover, its area appears to be much larger than in the optimal cases.(see Figure 3.6)

Conversely, if the capacitance is too large, the Lissajous curve becomes very flat and horizontally elongated, and is characterized by a high level of noise. If such a capacitance were used to compute the power, a highly invasive signal filter would be required, which would compromise the accuracy of the results and at the same time invalidate the main advantages of this method over the use of instantaneous voltage and current measurements.

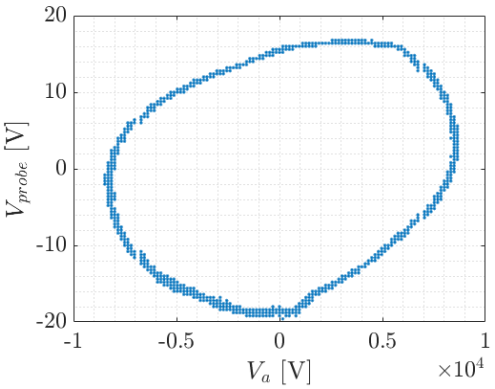

Figure 3.6: Lissajous curve for a low probe capacitance (10nF).

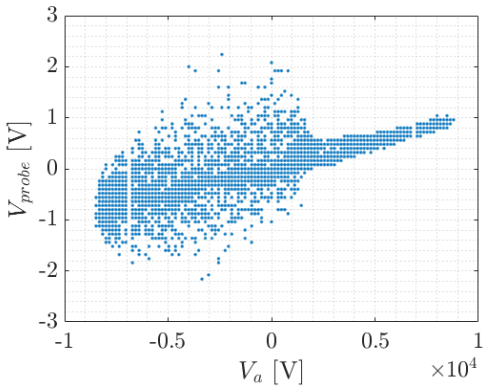

Figure 3.7: Lissajous curve for a high probe capacitance (5000nF).

The results of the analysis are shown in Figure 3.9. As previously mentioned, the area of the Lissajous curves is larger for small capacitance values and decreases sharply once an adequate capacitance is used. Due to a very big area of its corresponding Lissajous curve, a local peak in power consumption can be observed

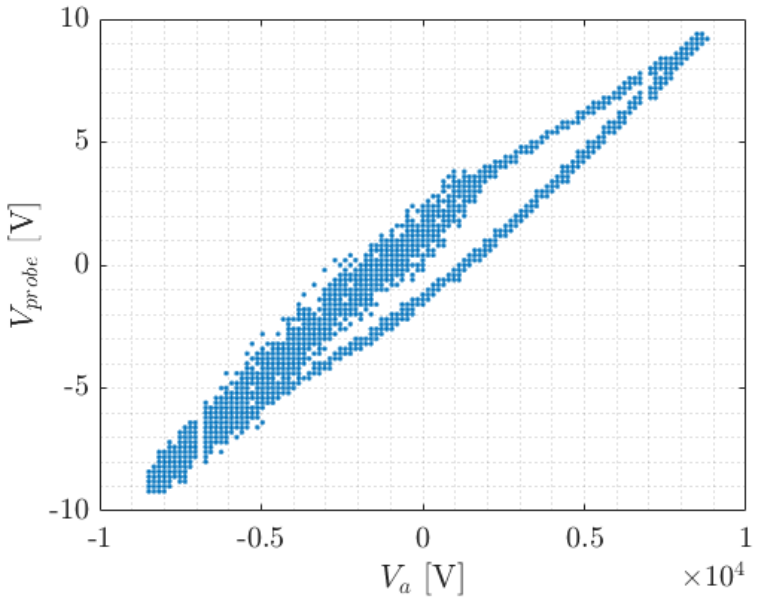

Figure 3.8: Lissajous curve for an optimal probe capacitance (300nF).

for $C = 100$ nF, while P_a appears to remain fairly constant within the range 200–700 nF. Therefore, the capacitance selected for the subsequent measurements belongs to this interval.

In the end, due to a better shaped - less noisy - Lissajous curve and the independence of measured consumed power from the capacitance, a probe capacitance of 300nF was selected for the real power consumption measurements.

3.1.3 Electrical performance

There seems to be an almost perfectly linear relation between voltage supplied and peak-to-peak voltage on our setup and the same can be said for the power consumed by the actuator while changing the voltage supplied. The electrical power efficiency of the system lies between 27.8% and 46.5%, reaching the latter value for $V_{supply} = 26$ V.
Finally, it is useful to calculate the power consumed for different peak-to-peak voltages, normalized with the plasma length, i.e., the actual extent of the plasma generated by the actuators.

From these measurements it emerges that the array consumes 96.1 W of electrical power (Figure 3.10), or 12.88 W/m of plasma in operating conditions (Figure 3.11).

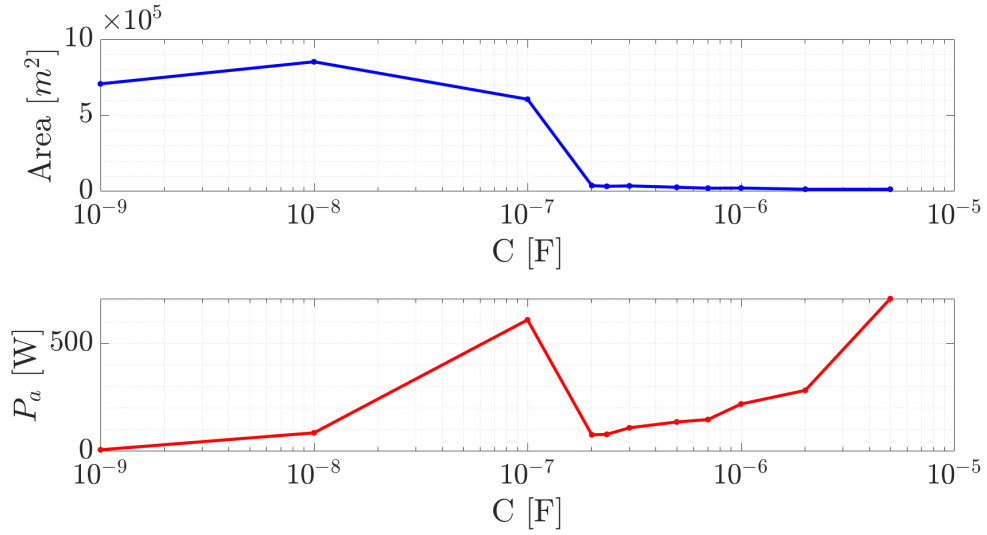

Figure 3.9: Area enclosed within the Lissajous curve for different C and resulting consumed power.

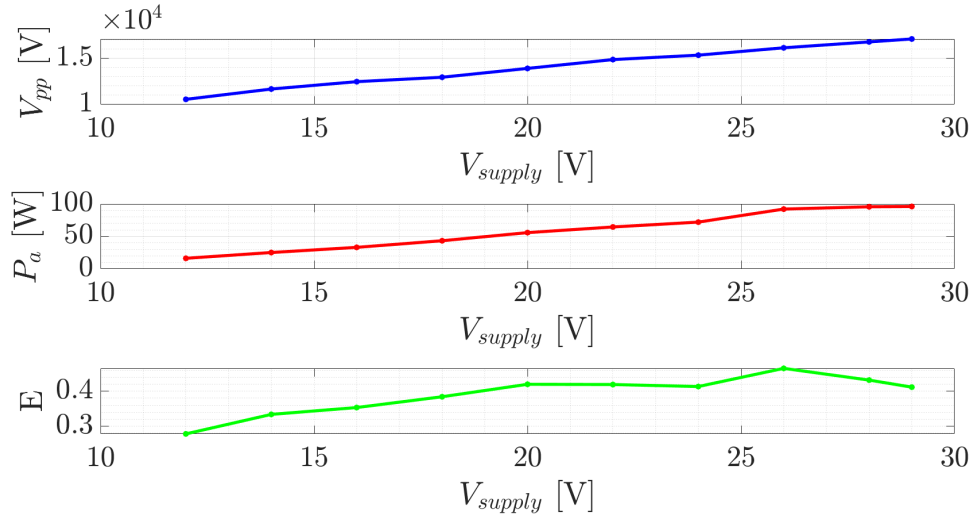

Figure 3.10: From the top: relation between voltage supplied and peak-to-peak voltage, power consumed for different V_{supply}, electrical efficiency

3.1.4 Electrical behavior in time

From Figure 3.12, it can be seen that, over the span of 3 minutes, the shape of the Lissajous curve changes slightly, representing a certain modification in electrical behavior. In fact, this can be seen from Figure 3.13 where a steady decline in input

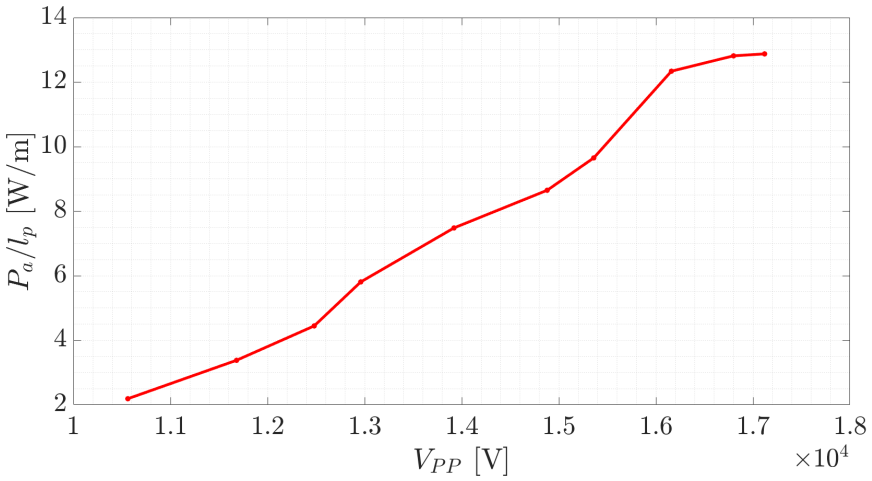

Figure 3.11: Consumed power scaled with plasma length, l_p.

current and input power absorbed by the actuator is clearly visible.

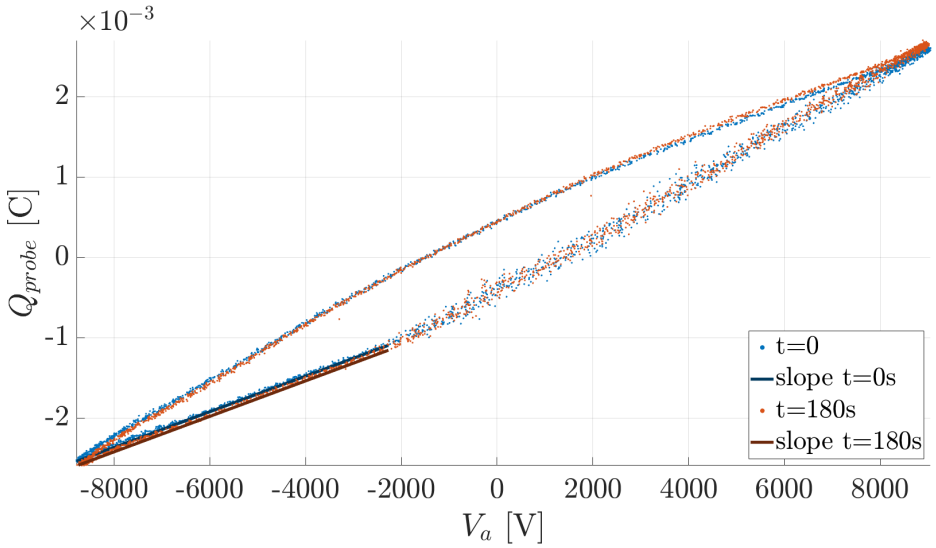

Figure 3.12: Lissajous curve obtained for t=0 s and for t=180 s, as well as the slope corresponding to the cold capacitance C_0 in the two cases.

In contrast, when computing the actual power consumed by the actuator P_a, the decreasing trend previously observed is no longer present. The quantities V_{pp}, P_a, and the electrical efficiency E appear to remain approximately constant over time, as shown in Figure 3.14.

As for the evaluation of C_0, the value of the cold capacitance also remains

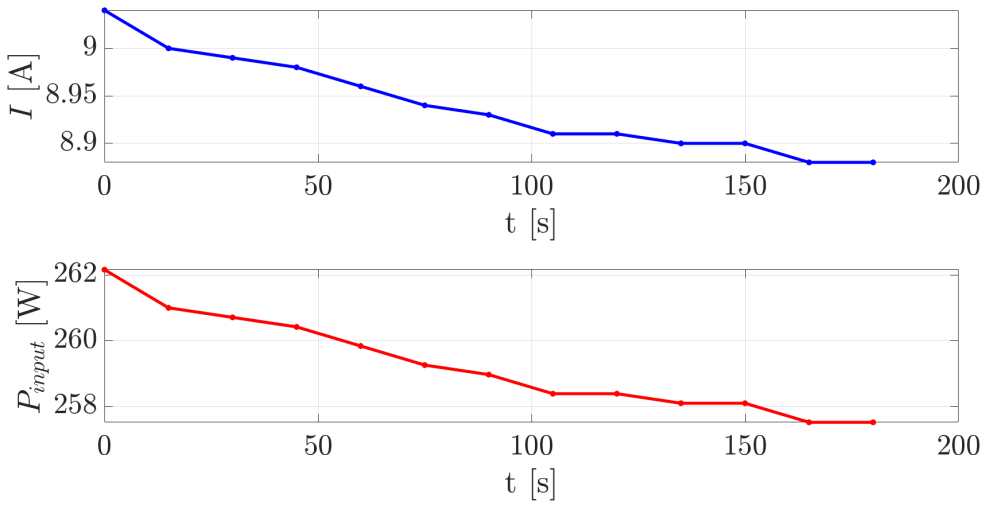

Figure 3.13: from the top: Input current I over the span of the experiment (180 s); input Power P_{input}.

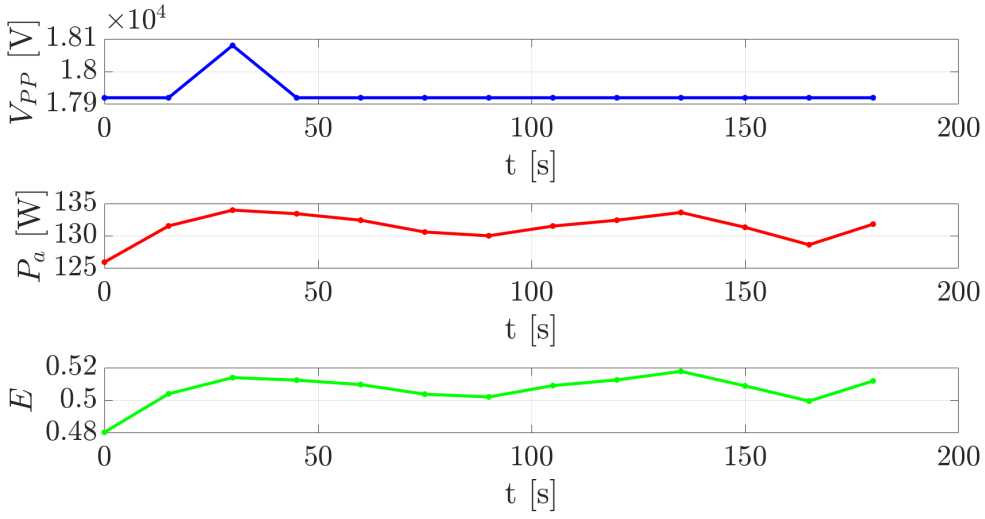

Figure 3.14: from the top: peak to peak voltage V_{PP}; consumed Power P_a; electrical efficiency E.

fairly constant in time (see Figure 3.15, top), with a maximum deviation of 2.2% from the computed mean value. However, after approximately 90 s of acquisition, wider oscillations were observed compared to the behavior recorded during the first seconds after actuation.

The standard deviation σ of the two measured electrical signals was calculated: the voltage across the shunt capacitor and the output signal from the high voltage source. The resulting standard deviation was found to decrease over time. It is therefore possible that the observed oscillations in the consumed power are not related to a less stable behavior of the actuator over time.

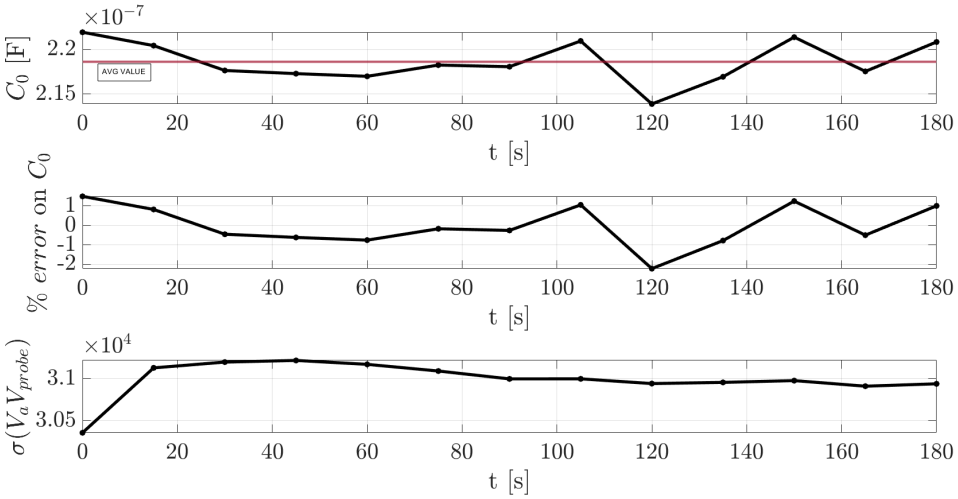

Figure 3.15: Top: cold capacitance C_0 and its time averaged value. Middle: percentile relative error on C_0 measurements ($\%error = \frac{C_0 - C_{0,mean}}{C_0}$). Bottom: standard deviation $\sigma(V_a V_{probe})$.

To more effectively assess the variation in time of the electrical behavior of the actuator array, it would be useful to take measurements over a time span one or two orders of magnitude longer, as done for example by Warlitz et al. [11]. However, this was not possible due to time constraints and to avoid wearing out or damaging actuators that may also be used in future drag-reduction measurements.

3.2 Mechanical characterization

In this section, the time-averaged velocity fields obtained from all the PIV snapshots will be presented. The flow fields and the maximum velocities reached in various part of the domain will first be examined, followed by an investigation of the thrust generated by the synthetic jets. Moreover, the differences arising from variations in the supply voltage V_{supply} will also be shown.

The following convention will be used for all the variables:

$$\mathbf{q}(x,y,z,t) = \mathbf{Q}(x,y,z) + \mathbf{q}'(x,y,z,t), \qquad \text{with} \qquad \mathbf{Q}(x,y,z) = \overline{\mathbf{q}(x,y,z,t)}.$$

Here, $\mathbf{q}$ denotes the instantaneous value of a generic thermodynamic variable, $\mathbf{Q}$ represents its time-averaged value, and $\mathbf{q}'$ indicates the corresponding instantaneous fluctuations. When an additional time average is needed for certain quantities, an extra $\overline{\mathbf{q}}$ symbol will be used to indicate it.

3.2.1 Velocity fields

In every analyzed plane of measure where the plane intersects the electrodes in the spanwise direction (planes A, B, C, see Figure 2.9), the most relevant velocity component field is the wall normal velocity V (Figure 3.16)

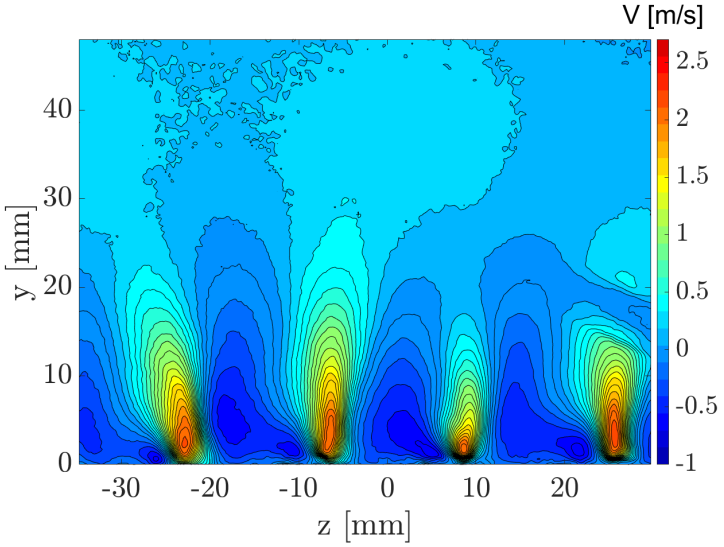

Figure 3.16: V velocity component for $V_{supply} = 26$ V, plane C.

The upwash motions, characterized by a positive wall normal velocity, V, are immediately evident, as well as the alternating mass-entrainment regions where

the wall-normal velocity is instead negative. These downwash regions are located directly above the electrodes, while the upwash regions are found halfway between two actuators, since it is caused by the collision of the wall jets generated by adjacent electrodes. From now on the upwash region will be called "plume".
Overall some of the velocity fields show a low spanwise symmetry, which is evident, for instance, in Figure 3.26, this is likely due to the fact that the plane of the actuators array deformed when the temperature increased as described in Section 2.3.

From the velocity fields it is possible to calculate the variation of V as a function of y at the location of the plumes for the different cases considered, and then perform an ensemble average to obtain the mean velocity profile V_{mean}, as illustrated in Figure 3.17 and 3.18:

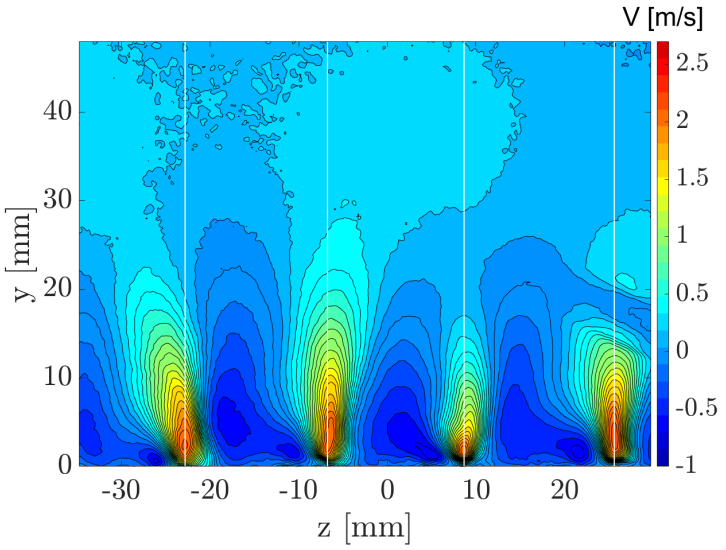

Figure 3.17: z location of the plumes. $V_{supply} = 26$ V, plane C.

The next step consists in comparing the velocity profiles obtained with $V_{supply} = 26\,\text{V}$ and $29\,\text{V}$. As shown in Figure 3.19, both for plane A and plane C it is found that, in the case of $V_{supply} = 29\,\text{V}$, the velocity peak is higher, and that, in both cases, it is located at $y = 2.1\,\text{mm}$ from the wall.

These comparisons cannot be made in plane B, as here the velocity field becomes much more irregular (Figure 3.20).

Different upwash and downwash regions can still be identified, but there are no more plumes. This can be attributed to the fact that the planes – A and B – previously considered intersect the sinusoidal electrodes at the positive and negative peak of the sine wave. This means that, locally, plasma only drives the surrounding

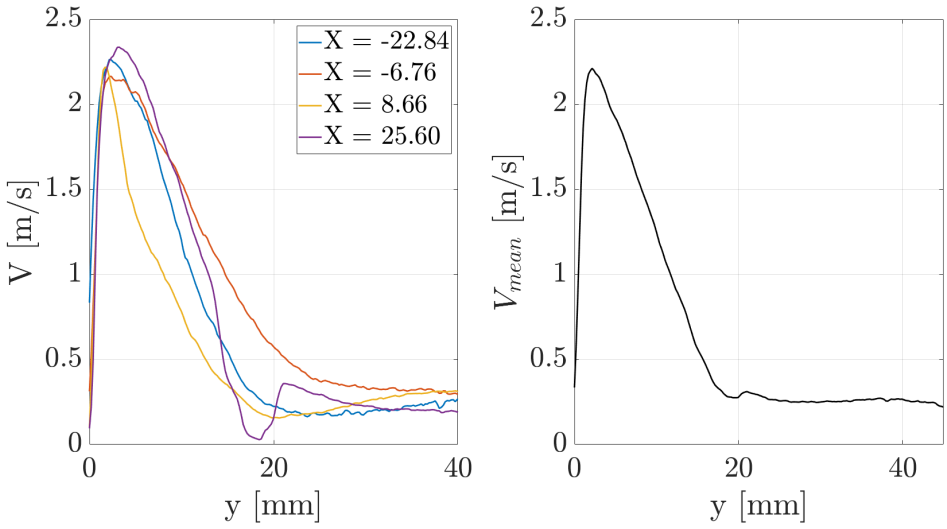

Figure 3.18: Left: $V(y)$ at the plumes location; right: $V(y)_{mean}$ along the spanwise direction, z. $V_{supply} = 26$ V, plane C.

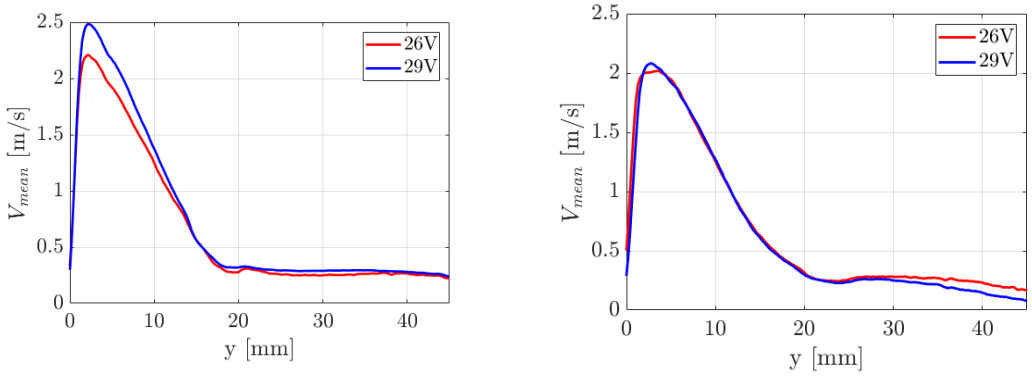

Figure 3.19: Comparison between $V(y)_{mean}$ at the plumes location for $V_{supply} = 26\,\text{V}$ and $V_{supply} = 29\,\text{V}$. On the left: plane C; on the right: plane A.

air in a direction parallel to the plane of measure. In plane B, however, since it is located between the other two, the effect of the actuators drives the fluid in a direction which is not parallel to plane B. As a result the maximum value of V decreases compared to plane A and C, together with the minimum value, signifying that most of the recirculation of air towards the exposed electrode happens within this plane. If this is the case also in presence of a mean streamwise flow, the flow might experience regions where the local skin friction coefficient is larger, due to the larger downwash motions located along plane B. The resulting velocity field

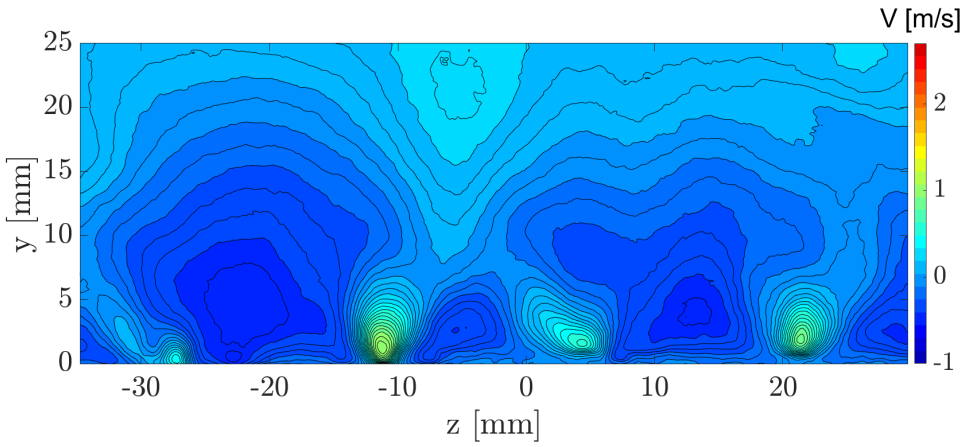

Figure 3.20: wall normal velocity component V for $V_{supply} = 26$ V, plane B.

might therefore present strong three-dimensional effects that have to be further investigated.

Another piece of information that can be extracted from the trend of the wall-normal velocity is the height of influence of the plume. Indeed, if we denote by $V(y)_{max}$ the maximum value reached by $V(y)_{mean}$, it is possible to define h_{jet} as the value of y for which:

$$V(h_{jet}) = \frac{1}{10} V(y)_{max}. \tag{3.1}$$

obtaining the following results:

V_{supply} [V]	26	29
h_{jet} [mm]	32.51	30.15

Table 3.2: h_{jet} measured for two operating conditions.

Contrary to what one might expect, the value of h_{jet} for $V_{supply} = 26$ V is greater than that obtained for $V_{\text{supply}} = 29$ V, although the two values remain fairly close to each other.

To confirm that, at $y = h_{\text{jet}}$, the fluid is no longer affected by the influence of the plume, the distributions $V(z)$ were computed at a few selected wall-normal

positions: the y location where $V_{\max}$ occurs, the height $y = h_{\text{jet}}$, and a third position halfway between these two.

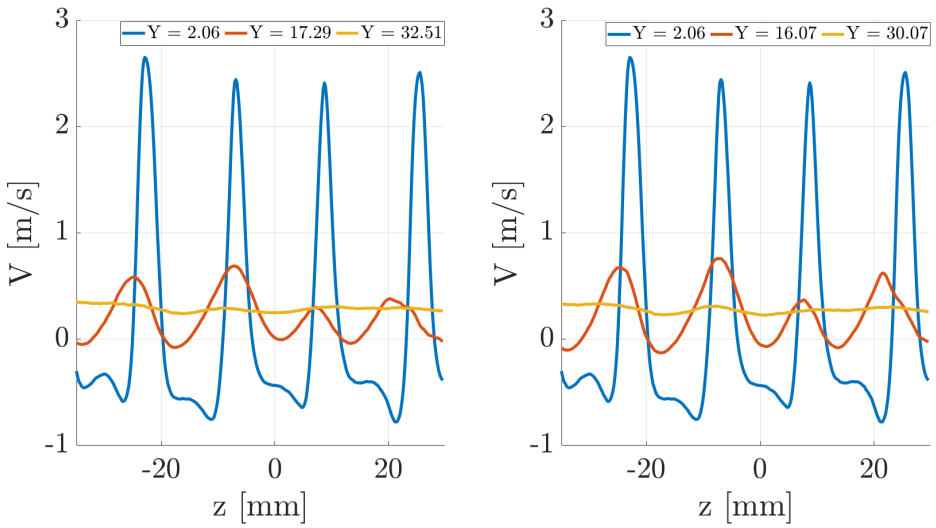

Figure 3.21: Comparison of V(x) at various wall normal positions. Left: V_{supply} = 26 V; right:V_{supply} = 29 V. plane C.

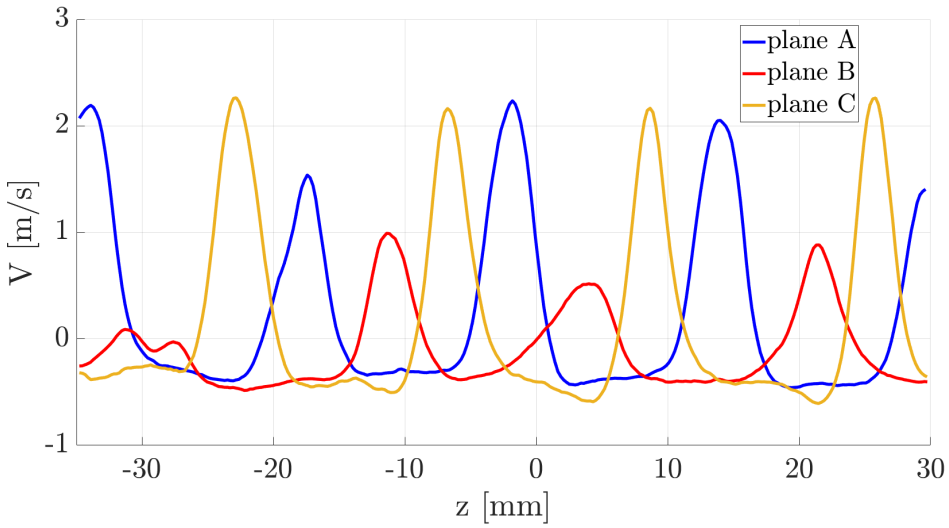

Figure 3.22: V peaks locations for measurement planes A, B and C.

From Figure 3.21 it is clearly visible the alternating pattern of upwash and downwash regions. Moreover, for $y = h_{jet}$ the velocity oscillations are practically

negligible, indicating that the influence of the plumes on the flow field has effectively vanished. It is worth noting, however, that in this region the wall-normal velocity remains positive. This is likely due to the significant heating generated by the actuators during operation, which may induce convective motions and an additional upward velocity component. The effect of this thermally–driven motion appears to persist even beyond the purely fluid–dynamic influence produced by the plasma-induced wall jets. Figure 3.22 illustrates where the different peaks of the wall normal velocity are located in every plane: A, B and C.

Regarding the spanwise velocity component W, the corresponding flow field is shown in Figure 3.23, which is representative of the situation observed in both measurement planes A and C.

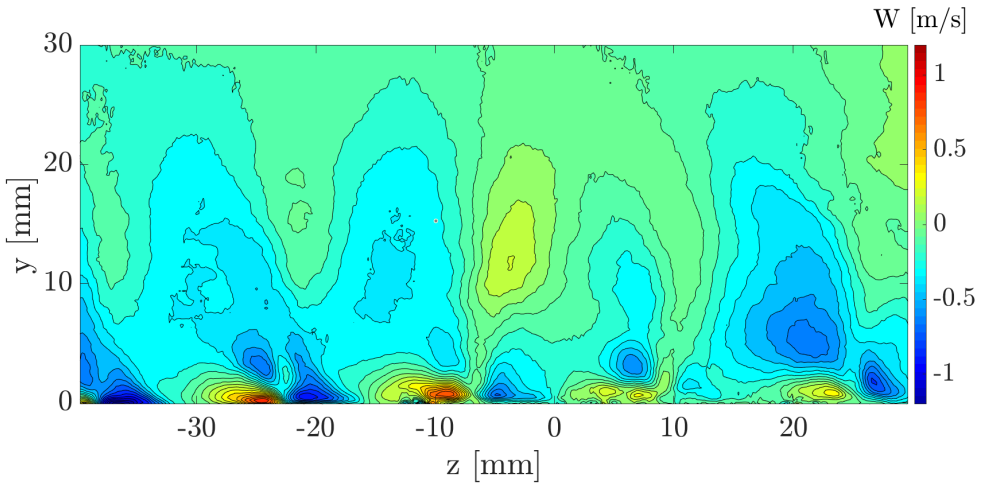

Figure 3.23: Spanwise velocity component W; $V_{supply} = 29$ V, plane C.

The wall jets generated by the actuators are clearly visible near the wall. However, their development in the spanwise direction is abruptly interrupted because they collide with the corresponding wall jet produced by the adjacent electrode, consequently altering the flow direction. It is precisely at these collision locations that the previously discussed plumes develop. It can also be observed that the maximum velocities reached by the spanwise velocity component W are lower than those measured for the wall-normal velocity component, reaching a maximum of 1.2 m/s. This further supports the idea that the jets do not fully develop in the spanwise direction, but predominantly in the wall-normal one. Directly above the wall jets, however, lies a region where the spanwise velocity seems to be directed in the opposite direction from the underlying jets. This means that from their

collision not only a plume is generated, but also a vortex, which can be clearly identified by computing the x component of vorticity in the field: Ω_x (Figure 3.24) and the Reynolds stress $\overline{v'w'}$ (Figure 3.25).

Vorticity is defined as:

$$\boldsymbol{\Omega} = \nabla \times \mathbf{U} \tag{3.2}$$

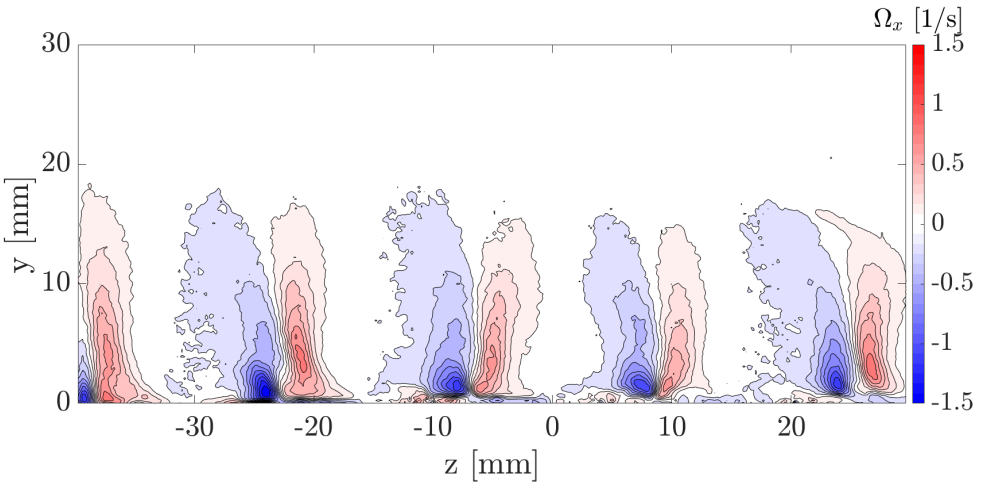

Figure 3.24: Vorticity Ω_x; $V_{supply} = 29$ V, plane C.

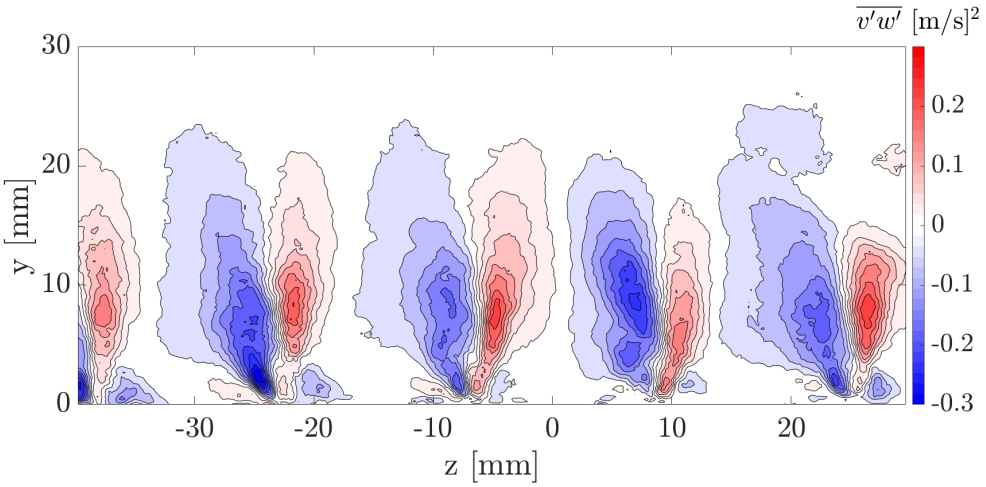

Figure 3.25: $\overline{v'w'}$ stress; $V_{supply} = 29$ V, plane C.

This time, for plane B, the flow field looks similar to what can be found in planes A and C. From Figure 3.26 the same wall jets can be identified, even though the induced velocity reaches a lower magnitude of 0.9 m/s maximum at the wall, and also the recirculation region above is clearly identifiable by opposite direction spanwise velocity from the underlying wall jets. This changes can, once again, be attributed to the direction in which the electrodes drive the surrounding air in plane B, which is in a direction not parallel to the plane of measure, resulting in a lower W measured.

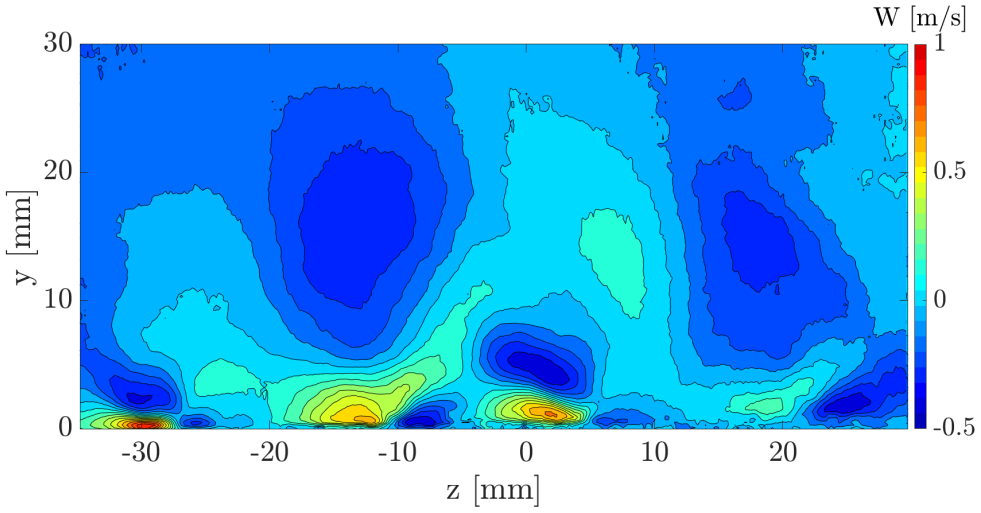

Figure 3.26: Spanwise velocity component W; $V_{supply} = 29$ V, plane B.

By plotting the vorticity Ω_x and the Reynolds stress $\overline{v'w'}$ in Figures 3.27 and 3.28 it is possible to notice that In plane B the vortices are much less developed than in planes A and C, especially in the wall normal direction, as they extend mainly close to the wall. The stress generated are also much smaller.

Finally, regarding the streamwise velocity component U, one might intuitively expect that, in planes A and C, this component would be close to zero, since each pair of actuators pushes the air in a direction parallel to the corresponding measurement plane. However, one must take into account the sinusoidal shape of the electrodes, which makes the flow field strongly three–dimensional. In fact, as shown in Figure 3.29, close to the wall an alternating pattern of positive and negative streamwise velocity can be observed.

If, as mentioned earlier, a significant portion of the recirculating motions toward the wall takes place within plane B, then the U velocity observed in planes A and C may be attributed to the movement of fluid from plane B toward these planes.

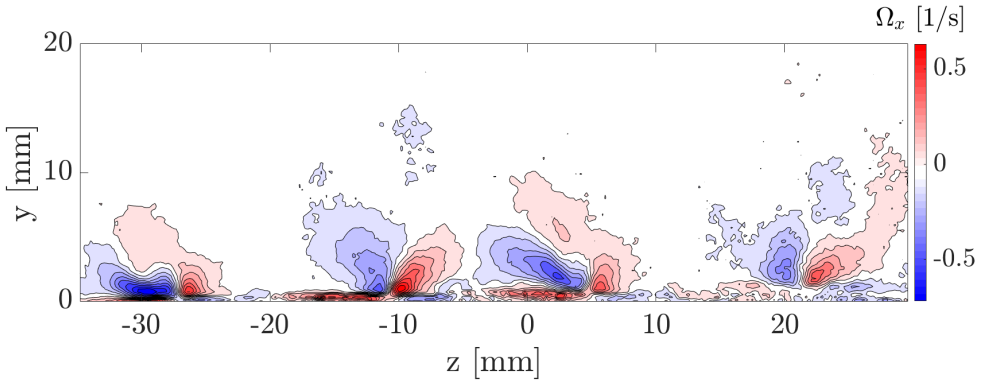

Figure 3.27: vorticity Ω_x; $V_{supply} = 29$ V, plane B.

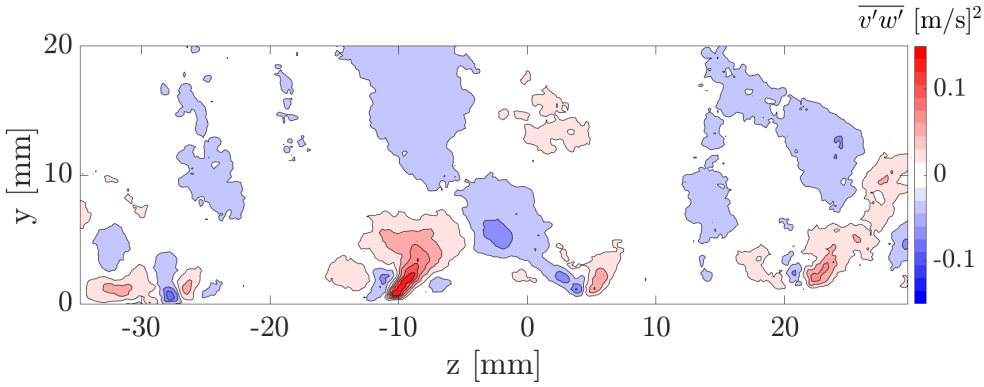

Figure 3.28: Stress $\overline{v'w'}$; $V_{supply} = 29$ V, plane B.

Focusing now on planes D, which is the plane in the middle of two adjacent electrodes, and E, which cuts one electrode in its middle plane (see Figure 2.9).

Once again the most relevant flow-field features are those associated with the wall-normal velocity component. For plane D (Figure 3.30), the alternating regions characterized by positive and negative V appear, while in plane E (Figure 3.31)

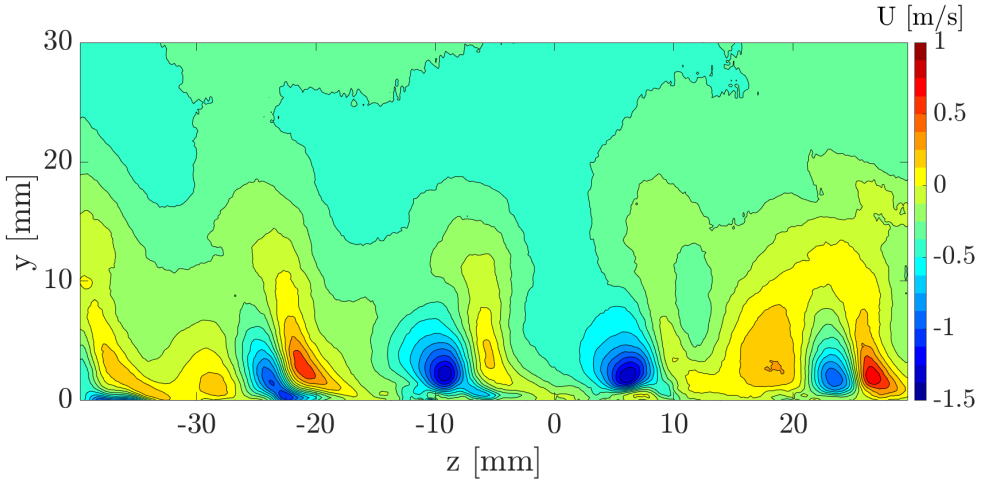

Figure 3.29: Streamwise velocity component U; $V_{supply} = 29$ V, plane C.

the previously observed plumes are again clearly visible. Once again, on top of the plumes, a non-zero wall normal velocity component is recorded, probably caused by thermally–driven convective flow motion. It is worth noting that the plume velocities are not constant from one plume to another. This is not due to any physical reason, but is most likely caused by a slight misalignment of the laser sheet, which was not perfectly centered to bisect the electrode into two equal halves.

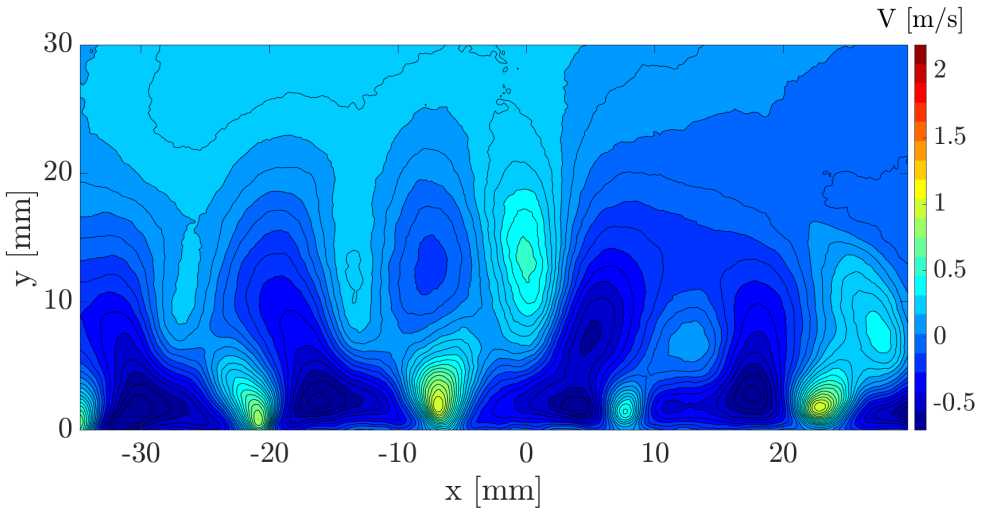

Figure 3.30: Wall normal velocity component V; $V_{supply} = 29$ V, plane E.

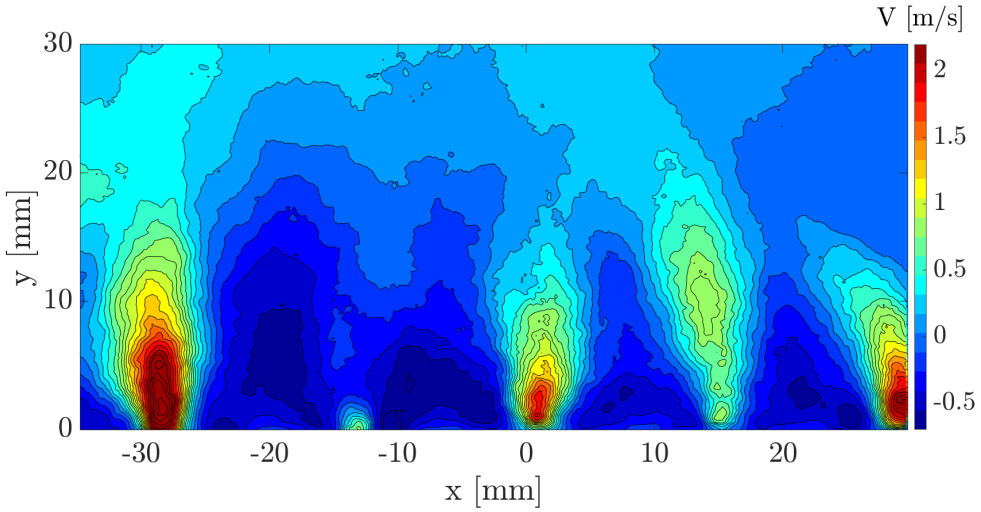

Figure 3.31: Wall normal velocity component V; $V_{supply} = 29$ V, plane D.

Another significant velocity field to consider is the one related to the spanwise velocity component W. As shown in Figure 2.9, the D plane intersects the maximum and minimum of two adjacent electrodes. In Figure 3.32, at the wall, it can be observed an alternation of regions with positive and negative W, generated by the wall jets produced by these electrodes. These regions show a characteristic "two-lobed" shape with lower velocity in the middle, precisely because the D plane

passes directly above the electrode surface, where no spanwise velocity is generated.

Above the wall-jet region, a large band, extending up to y=25 mm, is visible, where spanwise velocity is opposite to the respective jet below. This again indicates the presence of the vortical structures already observed in Figures 3.24 and 3.25.

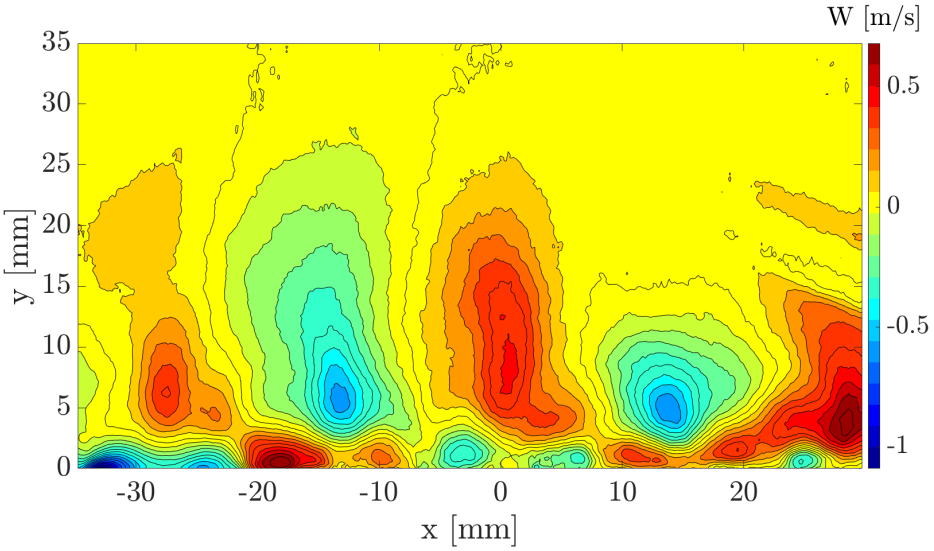

Figure 3.32: Spanwise velocity component W; $V_{supply} = 29$ V, plane D.

Taking into account plane E instead, the alternation of regions with positive and negative W observed in Figures 3.33 is caused by the effect of a single electrode. Since this electrode is intersected along its entire length at its midline (see Figure 2.9), it generates a positive spanwise velocity at the sinusoidal peaks and a negative one at the minimum points.

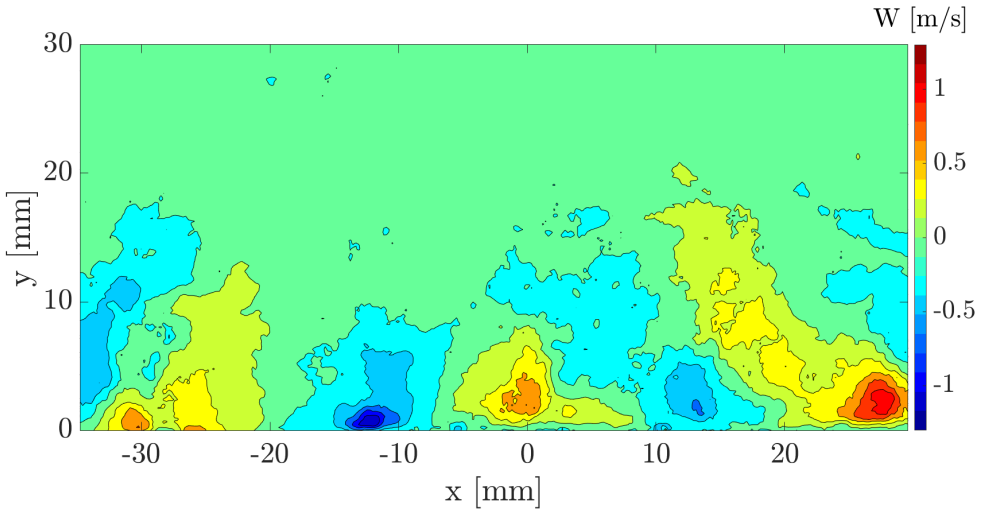

Figure 3.33: Spanwise velocity component W; $V_{supply} = 29$ V, plane E.

3.2.2 Thrust evaluation

In order to calculate the thrust generated by the actuators in both the wall-normal and spanwise directions, the method proposed by Kotsonis et al. [6] (and described in Section 1.3.3) was employed, although with some modifications required to adapt it to our specific configuration. In fact, in our case, it is not possible to perform a momentum balance on a single isolated actuator, since in an actuator array each device is affected by the presence and the influence of the adjacent actuators. It was therefore decided to compute the thrust induced by a pair of actuators. Since the main effect, resulting from the interaction between two adjacent actuators, is the formation of the plume, the control volume was chosen so as to enclose the region of space where this upwash motion is found. It should be noted, however, that with this approach it is not possible to place the boundaries of the control volume sufficiently far from the bulk of the body force generated by the actuators to assume the pressure to be equal and uniform over all its surfaces. This implies that, in the calculated thrust, the contribution due to pressure will be neglected. Nevertheless, this term remains secondary when compared to the contribution associated with the momentum flux. Moreover the domain is symmetric with respect to the electrodes pair and as such we can assume a similar pressure contribution on the two sides at constant z, which therefore can be assumed to cancel out. The velocity fields used for the thrust calculation are those corresponding to measurement plane C, although the results are equivalent to those obtained for plane A.

To assess the influence of the control volume dimension on the estimated thrust, control volumes with progressively increasing height will be employed.

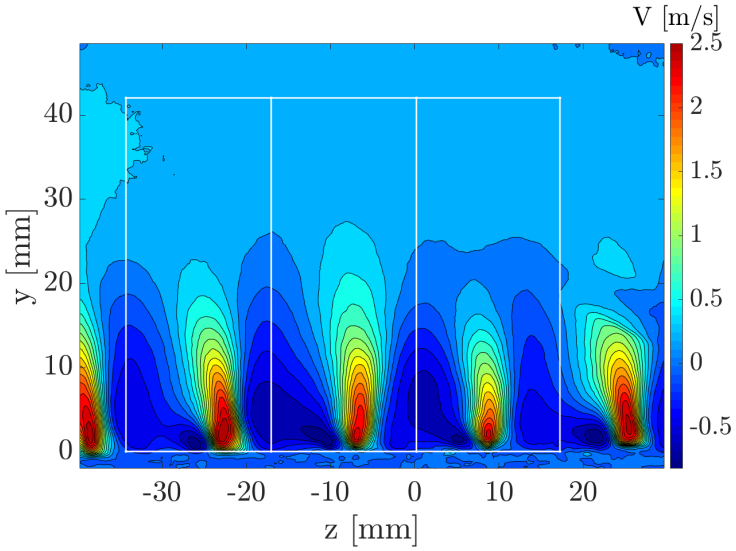

Figure 3.34: Maximum extension of the control volumes employed in thrust calculation; $V_{\text{supply}} = 29$ V, plane C.

Unfortunately, due to the close spacing between the electrodes, it is not possible to widen the volume in the z direction, as this would cause the control volume to enter the region of influence of the adjacent actuator. Moreover, three control volumes will be employed, each one corresponding to a different plume. The thrust values obtained from these volumes will then be averaged in order to provide a more reliable estimate of the generated thrust.

Figure 3.34 shows the control volumes of maximum dimension used in the case of $V_{\text{supply}} = 29$ V, but they are the same to those employed for $V_{\text{supply}} = 26$ V, so as to ensure full comparability of the results. The contribution given by the bottom of the control volume has been neglected in every case, since because of the non slip condition, there is no momentum flux on this surface.

The results obtained for $V_{\text{supply}} = 29$ V and $V_{\text{supply}} = 26$ V are reported in Figures 3.36 and 3.36, respectively.

In all cases considered, both for T_z and T_y, it appears that after a certain height h, around 20 mm, the thrust trends tend to stabilize. Furthermore, the trend of T_y is similar for each plume, whereas for T_x this is not necessarily the case; in fact, some curves are monotonically increasing while others are decreasing. However, this phenomenon is easily understood, as a higher-than-average outgoing momentum flow in the spanwise direction exiting a control volume will correspondingly generate a higher-than-average incoming momentum flow in the adjacent control volume.

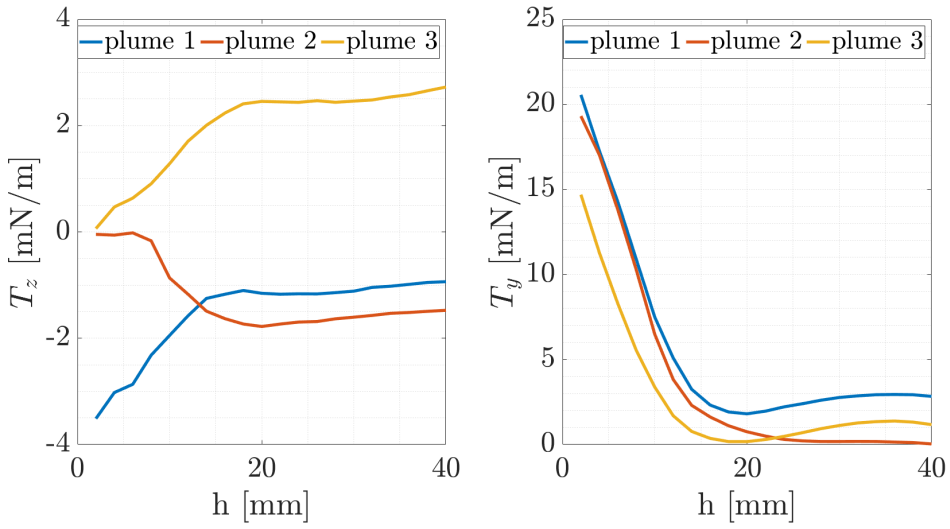

Figure 3.35: Trend of thrust components T_z and T_y as the control volume height h increases; $V_{\text{supply}} = 29$ V, plane C.

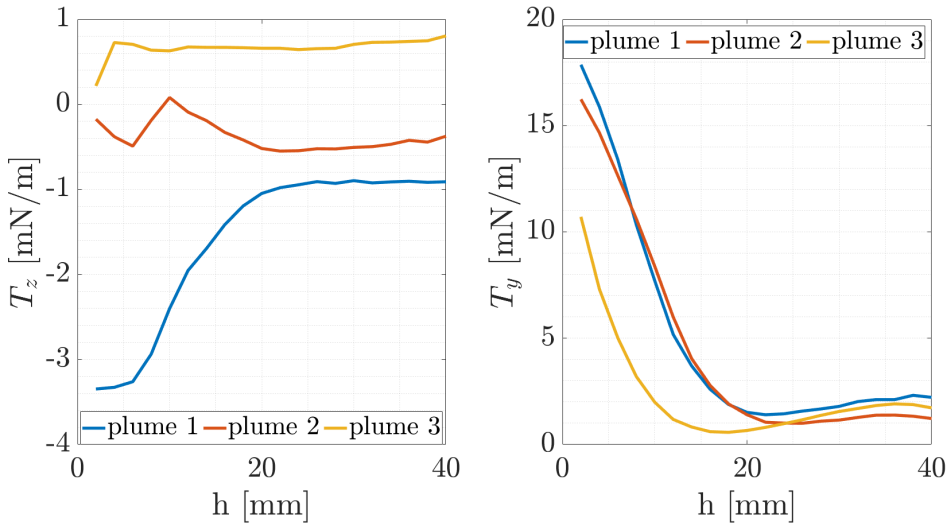

Figure 3.36: Trend of thrust components T_z and T_y as the control volume height h increases; $V_{\text{supply}} = 26$ V, plane C.

Looking now at the trends of T_z and T_y averaged over the three plumes considered (Figure 3.37), it can be observed that the spanwise component settles around zero for all cases, indicating that the thrust generated by each electrode is compensated by that of the adjacent electrodes. As a matter of fact, the actuator

array used has a symmetric behavior in the spanwise direction and so T_z was expected to be close to zero. Regarding the wall-normal thrust, for small h values, a higher thrust is recorded for $V_{supply} = 29$ V; however, this trend reverses starting from $h = 9.5$ mm. Beyond this point, the curves remain very close to each other, suggesting that the difference in voltage applied to the actuators is not sufficient to produce a significant variation of thrust in the y direction. This might be related to the fact that the actuator is not directly inducing a wall- normal velocity, but this velocity component is rather the result of two spanwise jets colliding, therefore a higher voltage does not appear to linearly increase the induced velocity as it is the case for other PAs configurations [7]

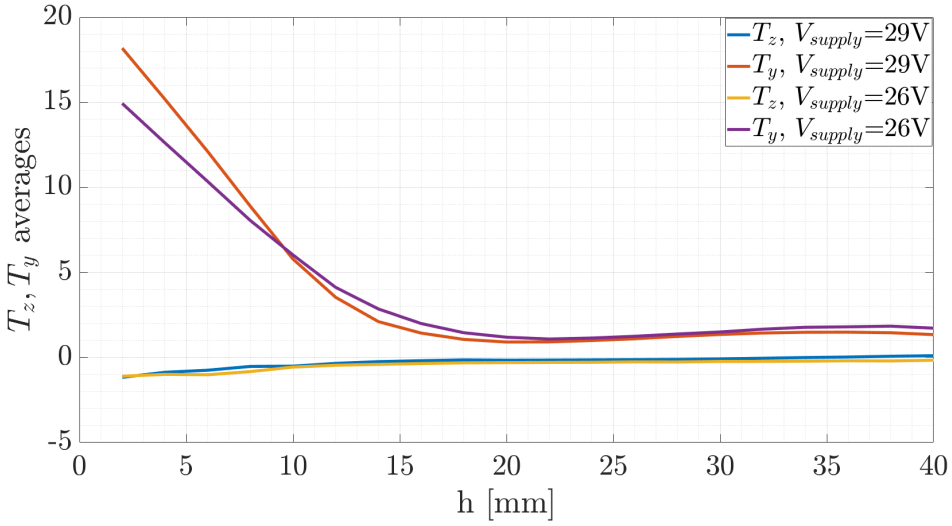

Figure 3.37: Trend of averaged thrust components T_z and T_y for every as the control volume height h increases.

In order to provide a representative value of the wall-normal thrust generated by a pair of actuators for both V_{supply} values, the height h was set to 32 mm, which is close to the dimension previously identified in Section 3.2.1 as h_{jet} , which represents the height at which the plumes' wall normal velocity decreases by 90%. The final results are reported in Table 3.3 and Figure 3.38.

.

V_{supply} [V]	T_z [mN/m]	T_y [mN/m]
26	-0.231	1.66
29	-0.044	1.44

Table 3.3: Thrust generated by a couple of adjacent electrodes in the spanwise and wall normal direction.

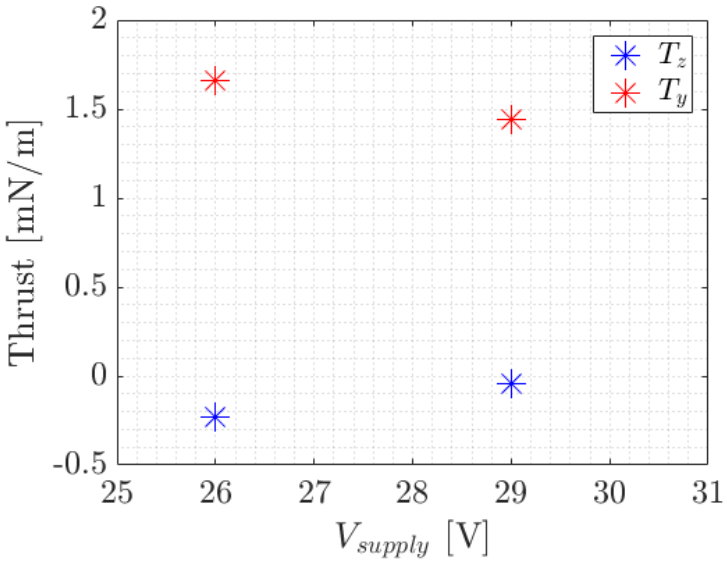

Figure 3.38: Values of T_z and T_y for different V_{supply}.

Chapter 4

Discussion

4.1 Conclusions

The objective of this thesis project was to build an array of DBD plasma actuators with a non conventional shape of the exposed electrodes, inspired by the work of Benard et al. [16]. A new fabrication process, which includes the use of an engraving laser to cut the stencil that shapes the electrodes, was successfully employed, and proved to be much more accurate and quicker for manufacturing actuators with complex geometries. Additionally, a new material for the dielectric layer was used, resulting in a sturdier, more durable device, capable of strong plasma generation, operated at a peak to peak voltage just shy of 20 kV.

The fabricated device was then electrically characterized, emphasizing the electrical power consumption for different actuation frequencies and voltage supplied values. The array was shown to be relatively efficient in generating plasma, consuming 96.1 W or 12.88 W/m of plasma under operating conditions.

The stereo PIV campaign that was later performed was useful in order to mechanically characterize the actuators. Images from different planes of measure were captured, allowing for a deeper understanding of the spatial evolution of the velocity field above the actuators. Particular attention was given to the wall-normal velocity field, since this is where the so-called "plumes" become clearly visible. These structures are characterized by a strong and concentrated velocity directed from the wall toward the outer flow regions, and are generated by the interaction between the wall jets produced by two adjacent electrodes. The strength of the plumes was studied in relation to the voltage supplied to the actuators and the resulting vorticose structures were observed.

Finally, the thrust generated by the actuators array was measured for two different values of supplied voltages. The results show that most of the thrust is produced in the wall normal direction, reaching 1.66 mN/m for a supplied voltage

of 26 V; while in the spanwise direction the value of generated thrust is basically negligible (at least in the inner region of the array, far away from the edges).

4.2 Outlooks

Although using 2-mm-thick polystyrene sheets as dielectric material represents a significant improvement compared to the initial 0.5-mm PET films, this material is still susceptible to bending when the actuator is operated for extended periods of time, especially at high supplied voltages. To further enhance the mechanical performance, one possible solution would be to replace polystyrene with a quartz or glass plate, which would also allow the actuator to withstand higher peak-to-peak voltages without the risk of dielectric breakdown.

A possible improvement concerning the electrical characterization would be to perform a long-term evaluation of the power consumption over time and of the corresponding variation of the cold capacitance C_0 of the actuators. In fact, in this study, the duration of the measurements was only about 3 minutes, but to obtain meaningful data it would be necessary to acquire measurements over a time scale of several hours, even though, admittedly, this may lead to damaging or compromising the actuators. Moreover, for large arrays such as the one investigated in this project, it may be beneficial to supply the actuators using more than one power supply and more than one high-voltage source, in order to deliver additional electrical power and avoid risking equipment damage by operating continuously at the imposed safety limits.

For the mechanical characterization and the PIV campaign, it would have been useful to acquire measurements over a larger range of supplied voltages, as well as to investigate the influence of the actuation frequency on the velocity fields. Moreover, a PIV setup in the wall-parallel x-y plane could further highlight the structures generated by the sinusoidal shape of the electrodes. Finally, to confirm the actual capability of the actuators to reduce skin-friction drag, a wind-tunnel measurement campaign in the presence of flow would represent the natural conclusion of the experiment.

Bibliography

[1] International Civil Aviation Organization (ICAO). *2025 ICAO Environmental Report*. Tech. rep. 2025 (cit. on p. 1).

[2] Stephen B. Pope. *Turbulent Flows*. cambridge university press, 2000 (cit. on pp. 4, 5).

[3] Gareth H Mckinley Shabnam Raayai-Ardakani. «Geometric optimization of riblet-textured surfaces for drag reduction in laminar boundary layer flows». In: *Physics of Fluids* (2019) (cit. on p. 6).

[4] Davide Gatti Marc T. Hehner and Jochen Kriegseis. «Stokes-layer formation under absence of moving parts—A novel oscillatory plasma actuator design for turbulent drag reduction». In: *Physics of Fluids* (2019) (cit. on pp. 7, 35).

[5] Pierre Ricco, Martin Skote, and Michael A. Leschziner. «A review of turbulent skin-friction drag reduction by near-wall transverse forcing». In: *Progress in Aerospace Sciences* (2021) (cit. on p. 7).

[6] L Veldhuis M Kotsonis S Ghaemi and F Scarano. «Measurement of the body force field of plasma actuators». In: *Journal of Physics D: Applied Physics* (2011) (cit. on pp. 8, 9, 12, 13, 70).

[7] Thomas C. Corke, C. Lon Enloe, and Stephen P. Wilkinson. «Dielectric Barrier Discharge Plasma Actuators for Flow Control». In: *The Annual Review of Fluid Mechanics* (2009) (cit. on pp. 9, 40, 73).

[8] S. Laizet O. Mahfoze. «Skin-friction drag reduction in a channel flow with streamwise-aligned plasma actuators». In: *International Journal of Heat and Fluid Flow* (2017) (cit. on p. 10).

[9] B. Dong, J. M. Bauchire, J. M. Pouvesle, P. Magnier, and D. Hong. «Experimental study of a DBD surface discharge for the active control of subsonic airflow». In: *J. Phys. D: Appl. Phys.* (2008) (cit. on p. 11).

[10] Marios Kotsonis. «Diagnostics for characterisation of plasma actuators». In: *Meas. Sci. Technol* (2015) (cit. on pp. 17, 18).

[11] Philipp Warlitz, Marc T. Hehner, Saskia Pasch, Jacopo Serpieri, Thomas Blank, and Jochen Kriegseis. «On durable materials for dielectric-barrier discharge plasma actuators». In: *Elsevier, Sensors and Actuators: A. Physical* (2023) (cit. on pp. 19, 43, 57).

[12] Jochen Kriegseis. «Performance Characterization and Quantification of Dielectric Barrier Discharge Plasma Actuators». PhD thesis. Technischen Universität Darmstadt, 2011 (cit. on p. 20).

[13] Graham A. Johnson Timothy N. Jukes Kwing-So Choi and Simon J. Scott. «Turbulent Drag Reduction by Surface Plasma through Spanwise Flow Oscillation». In: *3rd AIAA Flow Control Conference, San Francisco, California. American Institute of Aeronautics and Astronautics*. 5 - 8 June 2006 (cit. on pp. 21–23, 35).

[14] X.Q. Cheng, C.W. Wong, F. Hussain, W. Schröder, and Y. Zhou. «Flat plate drag reduction using plasma-generated streamwise vortices». In: *J. Fluid Mech.* (2021) (cit. on pp. 23–26, 35).

[15] Zhi SU, Haohua ZONG, Hua LIANG, Jun LI, Like XIE, Xuecheng LIU, Weiliang KONG, and Borui ZHENG. «Minimizing airfoil drag at low angles of attack with DBD-based turbulent drag reduction methods». In: *Chinese Journal of Aeronautics* (2022) (cit. on pp. 27–30).

[16] N. Benard, E. Moreau, and J.P. Bonnet. «Drag reduction by wall-parallel standing wave with plasma actuator». In: *AIAA SciTech Forum* (2024) (cit. on pp. 29, 31–36, 75).

[17] Pierre Ricco and Shengli Wu. «On the effects of lateral wall oscillations on a turbulent boundary layer». In: *Experimental Thermal and Fluid Science* (2004) (cit. on p. 32).

[18] F. M. Ricci. «Controllo attivo di un flusso turbolento tramite l'utilizzo di attuatori al plasma». MA thesis. Politecnico di Torino, 2023 (cit. on p. 41).

[19] Jochen Kriegseis, Benjamin Möller, Sven Grundmann, and Cameron Tropea. «Capacitance and power consumption quantification of dielectric barrier discharge (DBD) plasma actuators». In: *Journal of Electrostatics* (2011) (cit. on p. 52).